Ciliary length regulation by intraflagellar transport in zebrafish

Yi Sun[1,3,5], Zhe Chen[1,4,5], Minjun Jin[1,3], Haibo Xie[1,3,6], Chengtian Zhao[1,2,3,6]

[1]MOE Key Laboratory of Evolution & Marine Biodiversity and Institute of Evolution & Marine Biodiversity, Ocean University of China, Qingdao 266003, China

[2]Laboratory for Marine Biology and Biotechnology, Qingdao Marine Science and Technology Center, Qingdao, 266237, China

[3]Fang Zongxi Center for Marine Evo Devo, MOE Key Laboratory of Marine Genetics and Breeding, College of Marine Life Sciences, Ocean University of China, Qingdao 266003, China.

[4]Tsinghua-Peking Center for Life Sciences, Beijing Frontier Research Center for Biological Structure, McGovern Institute for Brain Research, State Key Laboratory of Membrane Biology, School of Life Sciences and MOE Key Laboratory for Protein Science, Tsinghua University, Beijing, China

[5]These authors contributed equally to this work.

[6]Corresponding author.

Haibo Xie

Email: xiehaibo@ouc.edu.cn

Chengtian Zhao

Email: chengtian_zhao@ouc.edu.cn

ABSTRACT

How cells regulate the size of their organelles remains a fundamental question in cell biology. Cilia, with their simple structure and surface localization, provide an ideal model for investigating organelle size control. However, most studies on cilia length regulation are primarily performed on several single-celled organisms. In contrast, the mechanism of length regulation in cilia across diverse cell types within multicellular organisms remains a mystery. Similar to humans, zebrafish contain diverse types of cilia with variable lengths. Taking advantage of the transparency of zebrafish embryos, we conducted a comprehensive investigation into intraflagellar transport (IFT), an essential process for ciliogenesis. By generating a transgenic line carrying Ift88-GFP transgene, we observed IFT in multiple types of cilia with varying lengths. Remarkably, cilia exhibited variable IFT speeds in different cell types, with longer cilia exhibiting faster IFT speeds. This increased IFT speed in longer cilia is likely not due to changes in common factors that regulate IFT, such as motor selection, BBSome proteins, or tubulin modification. Interestingly, longer cilia in the ear cristae tend to form larger IFT compared to shorter spinal cord cilia. Reducing the size of IFT particles by knocking down Ift88 slowed IFT speed and resulted in the formation of shorter cilia. Our study proposes an intriguing model of cilia length regulation via controlling IFT speed through the modulation of the size of the IFT complex. This discovery may provide further insights into our understanding of how organelle size is regulated in higher vertebrates.

INTRODUCTION

Understanding how cells regulate the size of their organelles is a fundamental question in cell biology. However, the three-dimensional complexity of most organelles poses challenges for accurate measurement, and thus, the underlying regulation mechanisms remain largely elusive. In contrast to the localization of most organelles within cells, cilia are microtubule-based structures that extend from the cell surface, facilitating a more straightforward quantification of their size. Cilia are highly conserved organelles found across various organisms, ranging from protozoa to humans. Their formation relies on microtubules, and their size can be easily measured by their length, making cilia an ideal model for studying size regulation of sub-cellular organelles within the same organisms(Chan & Marshall, 2012).

Cilia play a crucial role in regulating various physiological and biochemical processes(Goetz & Anderson, 2010, Nachury & Mick, 2019, Singla & Reiter, 2006). Structural or functional abnormalities of this organelle can result in a wide range of human genetic disorders, including retinal degeneration, polycystic kidneys, and mental retardation (Mill, Christensen et al., 2023, Reiter & Leroux, 2017, Song, Zhang et al., 2016). The assembly and maintenance of cilia rely on an elaborate process known as intraflagellar transport (IFT)(Kozminski, Johnson et al., 1993). The IFT complex is located between the doublet microtubules of the cilia and the ciliary membrane, playing a vital role as a mediator of cargo transportation within cilia(Bhogaraju, Cajanek et al., 2013, Hesketh, Mukhopadhyay et al., 2022, Meleppattu, Zhou et al., 2022). The IFT complex consists of two subcomplexes: the IFT-B complex, which transports the precursors required for cilia assembly from the base to the tip, powered by Kinesin-2; and the IFT-A complex, which transports axonemal turnover products back to the cell body by binding to dynein(Kardon & Vale, 2009, Ou, Koga et al., 2007, Scholey & J., 2008, Taschner, Bhogaraju et al., 2012). Electron microscopy studies have suggested that multiple IFT particles move together along the axoneme, earning the name "IFT trains"(Jordan, Diener et al., 2018, Kozminski, Beech et al., 1995, Stepanek & Pigino, 2016). In *Caenorhabditis elegans*, both the slow-speed heterotrimeric kinesin II and the

fast-speed homodimeric kinesin OSM-3 (mammalian ortholog, KIF17) coordinate IFT, ensuring the assembly of sensory cilia(Snow, Ou et al., 2004). The IFT system also interacts with the BBSome complex, dysfunction of which is associated with the human ciliopathy Bardet-Biedl syndrome(Tsang, Aycinena et al., 2018). The BBSome complex is moved by IFT and functions to maintain the physical connection between IFT-A and IFT-B subcomplexes in *C. elegans*(Ou, Blacque et al., 2005). Moreover, the BBSome is involved in diverse functions, including protein trafficking into and out of the cilia (Berbari, Lewis et al., 2008, Jin, White et al., 2010, Lechtreck, Johnson et al., 2009, Liu, Xue et al., 2021, Nachury, Loktev et al., 2007, Ye, Nager et al., 2018).

The intraflagellar transport system plays a crucial role in ciliogenesis and is highly conserved across various organisms. Interestingly, the length of cilia exhibits significant diversity in different models. For example, *Chlamydomonas* has two flagella with lengths ranging from 10 to 14 μm (Penny & Dutcher, 2024), while sensory cilia in *C. elegans* vary from approximately 1.5 μm to 7.5 μm (Snow et al., 2004). In most mammalian cells, the primary cilium typically measures between 3 and 10 μm (Han, Kang et al., 2014, Li, Yang et al., 2021, Tu, Li et al., 2023). Considering the conserved structure of cilia, it becomes intriguing to understand how their length is regulated in different cell types. Extensive research into flagellar length regulation has been conducted in *Chlamydomonas*. After one or two flagella are abscised, the shorter flagella can regenerate to their original length. During this regeneration process, the short flagella undergo a rapid growth phase, transitioning to a slower elongation phase as they approach their steady-state length(Rosenbaum, Moulder et al., 1969). IFT plays a central role in mediating flagellar regeneration and IFT particles usually assemble into 'long' and 'short' trains within the flagella. At the onset of flagellar growth, long trains are prevalent, while the number of short trains gradually increases as the flagellum elongates (Engel, Ludington et al., 2009, Vannuccini, Paccagnini et al., 2016). Moreover, the rate at which IFT trains enter the flagella, known as the IFT injection rate, is negatively correlated with flagellar length during regeneration (Engel et al.,

2009, Ludington, Wemmer et al., 2013). Researchers have proposed and tested several theoretical models to explain the regulatory mechanism of the IFT injection rate (Ishikawa, Moore et al., 2023, Marshall, 2023, Wemmer, Ludington et al., 2020). Intriguingly, recent studies in the parasitic protist Giardia, which possesses eight flagella of varying lengths, revealed that the ciliary tip localization of microtubule-depolymerizing kinesin-13 is inversely correlated with flagellar length, similar to its role in flagellar length regulation (McInally et al., 2019; Piao et al., 2009; Wang et al., 2013). These findings add another layer of complexity to our understanding of ciliary length regulation and underscore the importance of investigating diverse model organisms to gain comprehensive insights into this fundamental biological process.

Notably, most studies on ciliary length control have focused on single-celled organisms. However, in vertebrates, the presence of highly diverse cell types results in cilia of varying lengths. Understanding how cilia length is regulated in different cell types and why such diversity exists is essential for comprehending the pathogenic mechanisms underlying various organ defects seen in ciliopathies. Unfortunately, direct observation of intraflagellar transport (IFT) in living vertebrates has posed challenges, limiting our knowledge in this area.

In this study, we capitalized on the benefits of embryonic transparency in zebrafish to explore dynamic IFT in various types of cilia. To the best of our knowledge, this is the first report of IFT investigation in multiple organs within a living organism. Our findings revealed a positive correlation between the speed of IFT transport and cilia length. Interestingly, in the cilia of crista and spinal canal, ultra-high-resolution microscopy suggested an association between ciliary length and the size of IFT fluorescent particles. Our data imply the presence of a novel regulatory mechanism governing IFT speed and ciliary length control in vertebrate cilia.

Results

Zebrafish provide an ideal model to compare ciliogenesis in different organs

Similar to humans, cilia are widely present in various organs in zebrafish. Utilizing an Arl13b-GFP transgene under the control of the beta-actin promoter, we can observe cilia in live embryos within organs such as Kupffer's vesicle, ear, lateral line, spinal cord, and skin. Cilia in the pronephric duct, olfactory pit, photoreceptor cells, and sperms can be visualized through antibody staining with acetylated-tubulin. Notably, the number and length of cilia exhibit significant variation across different tissues (Fig. 1). While most cells contain a single cilium, certain specialized cells, including those in olfactory epithelium and pronephric duct, form multicilia. In adult zebrafish, multiciliated cells can also be found in the brain ventricles (ependymal cells) and ovary(Liu, Xie et al., 2023, Ogino, Sawada et al., 2016). Consequently, zebrafish provides an ideal model for investigating ciliogenesis in diverse cell types(Leventea, Hazime et al., 2016, Song et al., 2016).

Rescue of *ovl* (*ift88*) mutants with *Tg(hsp70l: ift88-GFP)* transgene

To visualize IFT in zebrafish, we first generated a stable transgenic line, *Tg(hsp70l: ift88-GFP)*, which expresses a fusion protein of Ift88 and GFP under the control of the heat shock promoter (Fig. 2A). Ift88 plays a crucial role as a component of the IFT complex in maintaining ciliogenesis. Zebrafish *ovl* (***ift88***) mutants exhibited body curvature defects and typically do not survive beyond 7 days post-fertilization (dpf) (Tsujikawa & Malicki, 2004a). By performing a daily heat shock starting from 48 hours post-fertilization (hpf), we observed that the body curvature defects were completely rescued at 5dpf (Fig. 2B, C). Furthermore, we assessed ciliogenesis defects in these mutants. At 5 dpf, cilia were absent in most tissues of the *ovl* mutants (Fig. 2D). In contrast, this transgene effectively rescued ciliogenesis defects in all examined tissues (Fig. 2D and S1A). Interestingly, the GFP fluorescence of the transgene was prominently enriched in the cilia (Fig. 2D and S1A). Additionally, we conducted continuous heat shock experiments, which showed that *ovl* mutants carrying this

transgene were able to survive to adulthood (Fig. S1B). Taken together, these findings demonstrate that Ift88-GFP can substitute for endogenous Ift88 in promoting ciliogenesis.

Visualization of IFT in different cilia

The enrichment of Ift88-GFP within cilia implies that the *Tg(hsp70l: ift88-GFP)* transgene could serve as a valuable tool for real-time observation of IFT movement (Fig. 2D). For this purpose, wild type zebrafish embryos containing *Tg(hsp70l: ift88-GFP)* transgene were heat shocked at 37°C for 4 hours to induce the expression of Ift88-GFP either at 24 hpf or 4 dpf (Fig. S2A). Despite cilia typically being situated in the deep regions of the body, we successfully detected the movement of GFP fluorescence particles using a high-sensitive spinning-disc microscope. First, we focused on ear cristae hair cell cilia which are longer and easy to detect. We succeeded in the direct visualization of the movement of fluorescent particles in these cilia (Movie S1). Kymograph analysis revealed bidirectional movement of the Ift88-GFP particles along the cilia axoneme (Fig. 3A), akin to IFT movements observed in other species(Kozminski et al., 1993, Orozco, Wedaman et al., 1999). Moreover, we also captured the dynamic movement of these Ift88-GFP particles in various cilia, including those of neuromasts, pronephric duct, spinal cord, and skin epidermal cells (Fig. 3B-E, Movies S2-5).

Increased IFT velocity in longer cilia

Next, we quantified the velocity and frequency of IFT using kymographs generated from recorded movies. Both manual and automatic tracking methods showed that the retrograde IFT exhibited higher speed compared to anterograde transport within each type of cilia (Fig. 3F-G, S2B-D), which is consistent with previous findings in *C. reinhardtii* and *C. elegans* (Iomini, Babaev-Khaimov et al., 2001, Signor, Wedaman et al., 1999, Snow et al., 2004). Surprisingly, we observed significant variability in IFT velocities among different cilia. In ear crista cilia, the average speed of anterograde IFT

was 0.68 μm/s, while in the cilia of neuromast hair cells, it decreased to 0.54 μm/s. In skin epidermal cilia and spinal canal cilia, the transport rates were further reduced to 0.42 μm/s and 0.33 μm/s, respectively. The pronephric duct cilia showed intermediate average anterograde IFT rates at 0.46 μm/s. Similarly, retrograde transport also displayed considerable variability, with ear crista and neuromast cilia exhibiting the highest speeds (1.55 μm/s and 1.47 μm/s, respectively). In contrast, cilia in the spinal canal showed the slowest IFT, with an average speed of 0.35 μm/s, which was less than one fourth of the speed observed in ear crista cilia (Fig. 3G).

Notably, both anterograde and retrograde IFT displayed remarkably high transport speeds in ear crista and neuromast cilia. We observed that these cilia were particularly longer compared to others. To investigate this correlation further, we compared ciliary length in different tissues and discovered a strong correlation between cilia length and IFT speeds (Fig. 3H, I). Specifically, longer cilia demonstrated faster IFT rates in both the anterograde and retrograde directions. Interestingly, longer cilia also have a higher frequency of fluorescent particles entering cilia (Fig. 3J). To validate this relationship further, we created an additional transgenic line, *Tg(βactin: tdTomato-ift43),* which allowed us to label Ift43, a constituent of the IFT-A complex. Through the analysis of Ift43 transport in this transgenic line, we reaffirmed that the tdTomato-Ift43 fluorescence particles also exhibited the highest transport speeds in ear crista cilia (Fig. S3).

In *C. elegans*, retrograde transport has been shown to exhibit a triphasic movement pattern (Yi, Li et al., 2017). We further plotted IFT particle's velocity along the entire length of crista cilia, which reveals that anterograde IFT maintains a relatively constant speed, whereas retrograde IFT undergoes a slight acceleration process when returning to the base (Fig. S2E). Next, we compared IFT velocities in cilia of varying lengths within the same ciliary type. In the crista cilia of 4 dpf zebrafish larvae, both longer and shorter cilia were observed (Fig. S4). Interestingly, IFT velocities were similar between

216 the longer and shorter cilia (Fig. S4). We also compared IFT movement in the same
217 type of cilia at different developmental stages. In larvae at 30 hpf or 4 dpf, the length
218 of cilia in epidermal cells is comparable. Similarly, single cilia in the pronephric duct
219 were similar between 30 hpf and 48 hpf zebrafish larvae. In both cases, IFT speed was
220 comparable between the two different stages (Fig. S5). Together, these findings suggest
221 that IFT speeds are more related to cell types in zebrafish, rather than the growth of
222 cilia or developmental stages.
223
224 **IFT speed remains unchanged in the absence of Kif17, Kif3b or Bbsome proteins**
225 To understand the potential mechanisms underlying the variation in IFT speeds among
226 different cilia, we initially focused on differences in motor proteins. In *C. elegans*, the
227 homodimeric kinesin-2, OSM-3, drives the IFT complex at a relatively higher speed
228 compared to the heterotrimeric Kinesin-2(Ou et al., 2005). We examined IFT in *kif17*
229 mutants, which carry a mutation of the fast homodimeric kinesin(Zhao, Omori et al.,
230 2012). In the absence of Kif17, the IFT speeds remained similar to those of control
231 larvae (Fig. 4A, B, S6, Movie S6, Table S1). Similarly, the IFT maintained regular speed
232 in the absence of Kif3b in the ear crista (Fig. 4A, B, Movie S7, Table S1), possibly due
233 to the redundant function of Kif3c in the heterotrimeric Kinesin-2(Zhao et al., 2012).
234 Additionally, we assessed IFT in the *bbs4* mutants, which has been proposed to affect
235 IFT movements both in nematodes and mice(Uytingco, Williams et al., 2019). Once
236 again, the Bbs4 mutation had little effect on IFT motility (Fig. 4A, B, S6, Movie S8,
237 Table S1).
238
239 **Tubulin modifications, ATP concentration and IFT**
240 The post-translational modifications of axonemal tubulins can affect the interaction
241 between microtubules and motor proteins, thereby regulating their dynamics(Hong,
242 Wang et al., 2018, Janke & Bulinski, 2011, O'Hagan, Silva et al., 2017, Sirajuddin, Rice
243 et al., 2014). Next, we asked whether tubulin modifications can affect IFT in zebrafish.
244 Ttll3 is a tubulin glycylase that are involved in the glycylation modification of ciliary

245 tubulin(Wloga, Webster et al., 2009). We generated zebrafish *ttll3* mutants and
246 identified a mutant allele with an 8bp insertion, which causes frameshift, resulting in a
247 significantly truncated Ttll3 protein without TTL domain (Fig. 4C, D). Immunostaining
248 with anti-monoglycylated or polyglycylated tubulin antibody revealed that the
249 glycylation modification was completely eliminated in all the cilia investigated (Fig.
250 4E and S7A, B). Surprisingly, there are no obviously defects in the number and length
251 of cilia in the mutants. The velocity of IFT within different cilia also appears unchanged
252 (Fig. 4F, Movie S9, Table S1). The beating pattern of cilia in the pronephric is similar
253 between control and mutant larvae (Fig. S7C-E). Moreover, the mutants were able to
254 survive to adulthood and there is no difference in the fertility or sperm motility between
255 mutants and control siblings, which is slightly different to those observed in mouse
256 mutants (Fig. S7F-H) (Gadadhar, Alvarez Viar et al., 2021).
257
258 Next, we investigated whether polyglutamylation of axonemal tubulins can regulate
259 IFT movement in zebrafish. First, we knocked down the expression of *ttll6*, which has
260 been shown earlier to reduce tubulin glutamylation and resulted in body curvature in
261 zebrafish (Fig. S8A, B)(Pathak, Austin et al., 2011). The efficiency of *ttll6* morpholinos
262 was confirmed via RT-PCR (reverse transcription-PCR), which showed the splicing
263 error of intron 12 when introduced the morpholinos (Fig. S8C, D). Interestingly, we
264 observed only minor differences in IFT velocity between *ttll6* morphants and control
265 groups (Fig. 4G, Table S1). Ccp5 is the major tubulin deglutamylase that regulates
266 glutamylation levels inside cilia (Pathak, Austin-Tse et al., 2014). Interestingly, the IFT
267 speeds exhibited only slight changes in *ccp5* morphants (Fig. 4G and S8E-H, Table S1).
268 Together, these results suggest that glycylation and glutamylation modification may
269 play relatively minor roles on IFT in zebrafish. Considering the big difference in the
270 IFT speed among different cilia, we think it is very unlikely such difference is caused
271 by different levels of tubulin glycylation or glutamylation modification.
272

The movement of kinesin and dynein motors relies on the energy derived from ATP hydrolysis. In vitro studies using molecular force clamp techniques have shown that increasing ATP concentration significantly enhances the speed of kinesin during cargo loading(Visscher, Schnitzer et al., 1999). We further examined whether the difference of IFT speeds was caused by variation of ATP concentration inside cilia. We generated an ATP reporter line, *Tg (βactin: arl13b-mRuby-iATPSnFR$^{1.0}$)*, which contains a ciliary localized ATP sensor, mRuby-iATPSnFR$^{1.0}$ driven by β-actin promotor (Fig. S9A-B)(Lobas, Tao et al., 2019). This ATP sensor utilizes relative fluorescence intensity to indicate the concentration of ATP. By measuring the ratio of mRuby red fluorescence to green fluorescence in the longer crista and shorter epidermal cilia, we compared relative ATP levels between these two types of cilia. Again, we found no difference in the ATP concentration between crista and epidermal cilia, suggesting that variation of ATP concentration was unlikely to be the cause of different IFT speed (Fig. S9C).

Larger IFT particles are present in longer cilia

Finally, we aim to investigate the size of IFT particles within different type of cilia. In the flagellar of *Chlamydomonas*, IFT particles are usually transported as IFT trains, consisting of multiple IFT-A and IFT-B repeating subcomplexes and the kinesin-2 and IFT dynein motors. However, with current technique, it is unfeasible to distinguish the size of IFT trains on different type of cilia through ultra-structure electron microscopy in zebrafish. Instead, we sought to compare the size of the fluorescence particles using STED ultra-high-resolution microscopy. With this method, we were able to identify single IFT fluorescence particles with relatively high resolution. Compared with regular spinning disk data, the number of IFT fluorescence particles was significantly increased in the cilia (Fig. 5A, B). When comparing the size of these fluorescence particles, we found that the particle sizes were significantly larger in the longer crista cilia than those of the shorter spinal cord cilia (Fig. 5C).

To further test whether the higher IFT velocity was associated with large IFT particles in the crista cilia, we performed morpholino based knockdown analysis. Injection of *ift88* morpholino caused body curvature due to ciliogenesis defects (Fig. 5D). When injecting lower dose of *ift88* morpholino, we found zebrafish embryos can still maintain grossly normal body axis, while cilia in ear crista became significantly shorter (Fig. 5D, E, I). Due to partial loss of Ift88 proteins, the number of IFT complex decreased significantly as suggested by the reduced number of IFT fluorescence particles in the morphant cilia (Fig. 5F, G). Strikingly, the size of the fluorescent particles also decreased significantly (Fig. 5F, H). Moreover, the average intensity and size of fluorescent particles showed a strong correlation in both control and *ift88* morphants, which implies a potentially reduced length of the IFT trains (Fig. 5I). Interestingly, we found the IFT speed also decreased significantly in the shorter cilia (1.55 μm/s in control vs 1.18 μm/s in morphants) (Fig. 5J, K, Movie S10). Taken together, these data imply that the size of IFT fluorescence particles is related to IFT speed and longer cilia are prone to contain larger IFT particles than shorter cilia.

Discussion

With its diverse array of cilia types, zebrafish provide an exceptional model for investigating the intricate mechanisms underlying ciliary length regulation. By creating a transgenic line that expresses ciliary-targeted IFT proteins, we have demonstrated a positive correlation between IFT speed and the length of cilia. To the best of our knowledge, this study represents the first instance of comparing IFT in cilia from different types of organs within the same organism. Interestingly, the relationship between ciliary length and IFT speed has been studied recently in *Chlamydomonas,* which suggested that reduction of the IFT speed with chimeric CrKinesin-II can affect ciliary assembly activity, together with the formation of slightly shorter flagella (Li, Wan et al., 2020).

Surprisingly, certain conventional factors known to govern IFT transport regulation in *C. elegans* or *Chlamydomonas* appear to exert limited influence in zebrafish. IFT transport speed showed no discernible connection to ciliary motility, as evidenced by the comparable IFT speeds observed in both motile spinal cord cilia and primary cilia of the skin's epidermal cells (Fig. 3). Furthermore, IFT remains largely unchanged in mutants of *kif3b*, *kif17*, *bbs4*, or *ttll3*. In *kif3b* mutants, Kif3c may substitute for Kif3b to ensure proper IFT (Zhao et al., 2012). Although both KIF17 (OSM-3) and BBSome proteins have been shown to mediate IFT transport in the cilia of olfactory neurons in both nematodes and mice (Ou et al., 2005, Uytingco et al., 2019, Williams, McIntyre et al., 2014), it is still questionable whether these proteins can affect IFT in other types of cilia. Our data suggest that IFT velocity was not altered in the crista or neuromast cilia of *kif17* or *bbs4* mutants, consistent with the fact that Kif17 and BBSome proteins are dispensable for ciliogenesis in these tissues. Unfortunately, we couldn't detect IFT trafficking in the olfactory neurons of zebrafish with current techniques. It would be worthwhile to improve detection methods to determine whether the role of Kif17 or BBSome proteins is conserved during the ciliogenesis of olfactory neurons. Finally, although tubulin modifications are essential for IFT in C. elegans, IFT remains unchanged in *ttll3* mutants, in which tubulin glycylation is completely removed. Similarly, modification of tubulin glutamylation levels has minor effects on the movement of IFT. Collectively, these results suggest that the regulation of IFT velocity in zebrafish cilia differs from that observed in C. elegans and mice OSNs, thereby highlighting the intricate complexity of IFT regulation across various organisms.

Remarkably, our studies revealed that the IFT fluorescence particles were significantly larger in longer crista cilia than those of shorter cilia. The IFT complex typically travels as trains, with multiple repeating IFT units being transported simultaneously. The increased size of the fluorescence particles implies that longer cilia might form larger IFT trains for more effective cargo transportation. Decreasing the quantity of IFT88 proteins could diminish the likelihood of IFT complex assembly, consequently leading

358 to a reduction in the size of IFT trains. Importantly, the size of IFT particles was
359 significantly reduced in *ift88* morphants, concurrent with the decreased transport speed
360 of IFT. Thus, our data support a length control model for cilia that operates through the
361 modulation of IFT train size (Fig. 5L). Within longer cilia, the IFT complex appears
362 predisposed to form lengthier repeating units, thereby creating an optimal platform for
363 efficient transport. This environment enhances the coordination between cargos and
364 motor proteins, resulting in an improved transportation speed. This orchestration
365 potentially involves the synchronization of motor proteins, ensuring their precise
366 functionality and directional alignment during transport—a concept supported by
367 various models(Stukalin, Phillips et al., 2005, Urnavicius, Lau et al., 2018).
368 Furthermore, insights from the cryo-EM structure of intraflagellar transport trains have
369 suggested that each dynein motor might propel multiple IFT complexes. For instance,
370 the ratio of dynein: IFT-B: IFT-A in the flagella of *Chlamydomonas* is approximately
371 2:8:4(Jordan et al., 2018). It remains plausible that longer cilia in vertebrates could
372 recruit a higher ratio of motor proteins to execute IFT, thus intensifying the driving
373 force for cargo transport.
374
375 Finally, we want to mention that this study has several potential limitations. For instance,
376 the evaluation of IFT particle sizes was based on immunostaining results acquired from
377 STED microscopy, and we cannot distinguish between anterograde or retrograde IFT
378 transport as can be done with live imaging. It remains unclear whether IFT particles are
379 larger in both directions. Moreover, the size difference of IFT particles was only
380 compared between crista and spinal cord cilia. Due to technical issues, many cilia, such
381 as those in epidermal cells, were difficult to identify under high magnifications. It
382 would be helpful to isolate these cilia and perform ultrastructural analysis to compare
383 IFT train sizes between different types of cilia. Additionally, although IFT speed was
384 largely normal in the absence of Kif3b, Bbs4, and tubulin glycylation modification, it
385 remains possible that other factors, such as the presence of different adaptor proteins in

different cell types or the use of different tubulin codes, are involved in mediating IFT. The mechanisms behind these conditions may require further investigation.

In summary, due to their relatively simple structure and ease of measurement, cilia provide an excellent model for investigating the mechanisms of organelle size control. Our results indicate that cilia in zebrafish vary in length, and this length is closely related to cell types. Longer cilia may form larger IFT trains for faster transport to maintain their stability. It is possible that a larger IFT pool is present in the base region of longer cilia, which help assemble large IFT trains. The increased frequency of IFT transport in longer cilia further supports this concept. Comparing the expression levels of IFT and motor proteins across different cell types will be helpful in elucidating the differences in IFT injection rates among these cilia. Interestingly, the relationship between IFT transport velocity and cell type is also observed in other cell types, such as mouse olfactory neurons. In these neurons, cilia of the same type maintain similar IFT velocities, while different types of olfactory neurons exhibit significant variations (Williams et al., 2014). Investigating the IFT velocity within different cilia in mouse models in the future will be valuable.

Materials and methods

Ethics statement

All zebrafish study was conducted according standard animal guidelines and approved by the Animal Care Committee of Ocean University of China (Animal protocol number: OUC2012316).

Zebrafish Strains

Zebrafish Tuebingen (TU) strains were maintained at 28°C on a 14-hour/10-hour light/dark cycle. Embryos were raised at 28.5°C in E3 medium (5 mM NaCl, 0.17 mM KCl, 0.39 mM CaCl2, 0.67 mM MgSO4). The following mutant strains were used: *ovl*(Tsujikawa & Malicki, 2004a), *kif3b* and *kif17*(Zhao et al., 2012). Three transgenic

lines, *Tg(hsp70l:ift88-GFP), Tg(βactin:tdTomato-ift43)* and *Tg(βactin: arl13b-mRuby-iATPSnFR$^{1.0}$),* were generated in this study. The constructs for making these transgene were created using Tol2 kit Gateway-based cloning(Kwan, Fujimoto et al., 2007). The *ttll3* mutants were generated via CRISPR/Cas9 technology with the following target sequence: 5'-GGGTGGAGCGGCGATTGCCA-3'. The *bbs4* mutants were generated by TALEN system with the following binding sequences: 5'-TAAACTTGGCATTACAGC-3' and 5'- TCCCAGCATCATGTAGGTC -3'. All strains involved for analysis are stable lines.

IFT imaging

To prepare for time-lapse imaging, *Tg (hsp70l: ift88-GFP)* embryos were subjected to single heat shock treatment for 4 hours at 37 °C at either 24 hpf or 4dpf (Fig S2A). Then zebrafish embryos were raised at 28.5°C in fresh E3 medium for another 2-4 hours to obtain brighter fluorescence and higher signal to noise ratio. For living imaging, we used 35 mm glass-bottom dishes (FD35-100, WPI) filled with a thin layer of 3% agarose. Once the agarose solidified, several rectangle slots were cut out from dish using a capillary pipette. Zebrafish larvae were anesthetized with E3 water containing 0.01% Tricaine, and put into slots. After removing excess water, 1% low melting point agarose was added to cover the embryos. Finally, E3 water containing 0.01% Tricaine was added to the dish. IFT movement in cilia of crista and neuromast were recorded using an Olympus IX83 microscope equipped with a 60X, 1.3 NA objective lens, an EMCCD camera (iXon+ DU-897D-C00-#BV-500; Andor Technology) and a spinning disk confocal scan head (CSU-X1 Spinning Disk Unit; Yokogawa Electric Corporation). Time-lapse images were continuously collected with 100 or 200 repeats using μManager (https://www.micro-manager.org) at an exposure time of 200 ms. IFT movement in cilia of epidermal cells, spinal cord, and pronephric duct epithelial cells were recorded using an Olympus IX83 microscope equipped with a 100X, 1.49 NA objective lens, and the same EMCCD camera and spinning disk confocal modules as

443 mentioned above. We usually collected IFT images within 5 minutes after embedding
444 and only single focal plane images were used for analysis.
445
446 **Image processing and analysis**
447 ImageJ software was used to generate kymographs for quantifying cilium length and
448 velocity. To analyze IFT velocity, we employed an established method as previously
449 described(Zhou, Brust-Mascher et al., 2001). We first manually drew lines along the
450 cilia to define a track for detailed analysis of IFT velocity. Using a Fourier filtering
451 algorithm, the KymographClear plugin automatically color-coded anterograde and
452 retrograde particles. IFT velocities at different positions along the cilia were
453 automatically extracted using KymographDirect software and classified into groups at
454 2 μm intervals along the cilia. These velocities were then quantified to generate the
455 anterograde and retrograde velocity curves(Mangeol, Prevo et al., 2016).
456
457 **Whole-mount Immunofluorescence**
458 Zebrafish larvae were fixed overnight at 4°C in 4% PFA. After removing the fixative,
459 they were washed three times with PBS containing 0.5% Tween 20 (PBST) and then
460 incubated in acetone for 10 minutes for permeabilization. Subsequently, the embryos
461 were treated with a blocking reagent (PBD with 10% goat serum) for 1 hour and
462 sequentially labeled with primary and secondary antibodies (at a 1:500 dilution)
463 overnight at 4 °C. The following antibodies were used: anti-acetylated α-tubulin (Sigma
464 T6793), anti-SYCP3 (Abcam, ab150292), anti-monoglycylated tubulin antibody, clone
465 TAP 952 (Sigma MABS277), anti-polyglycylated tubulin antibody, clone AXO49
466 (Sigma MABS276), anti-GFP (Invitrogen A-11120), Alexa Fluor™ 633 phalloidin
467 (Invitrogen A22284), and zpr-1 (Zebrafish International Resource Center).
468
469 **Morpholino knockdown**
470 The following morpholinos were used: *ttll6* (5' – GCAACTGAATGACTTACTGAG-
471 TTTG - 3'), *ccp5* (5' -TCCTCTTAATGTGCAGATACCCGTT-3'), *ift88* (5' -

CAACTCCACTCACCCCATAAGCTGT - 3') (Tsujikawa & Malicki, 2004b) and a standard control morpholino (5' -CCTCTTACCTCAGTTACAATTTATA-3'). All morpholinos were purchased from Gene Tools (Philomath, OR). To detect splicing defects caused by morpholinos, we extracted total RNA from 24hpf embryos and performed RT-PCR using the following primer sequences: *ttll6* Forward: 5'-AAAGTATTTCCAACACAGCAGCTC-3', Reverse: 5'-GTGGTCGTGTCTGCAGTGTGGAGG-3'; *ccp5* Forward: 5'-TCCTGTCGTTTGTTCATCGTCTGC-3', Reverse: 5'-CTTAAAGACGAACATGC-GGCGAAG-3'.

Super-resolution microscopy

High resolution images were acquired using Abberior STEDYCON (Abberior Instruments GmbH, Göttingen, Germany) fluorescence microscope built on a motorized inverted microscope IX83 (Olympus UPlanXAPO 100x, NA1.45, Tokyo, Japan). The microscope is equipped with pulsed STED lasers at 775 nm, and with 561 nm and 640 nm excitation pulsed lasers. Zebrafish larvae were collected and fixed in 4% PFA overnight at 4°C, then processed for immunofluorescence with anti-GFP antibody and anti-monoglycylated tubulin antibody. For STED imaging, the following secondary antibody were used: goat anti-mouse Abberior STAR RED and goat anti-rabbit Abberior STAR ORANGE. The embryos were incubated in secondary antibody (1:100) in blocking buffer at room temperature for 2 h. After wash three times (5 min each) with PBST, larvae were cryoprotected in 30% sucrose overnight. Sagittal sections were collected continuously at 40 μm thickness on Leica CM1850 cryostat. Place the slices at 37°C for 1 hour to dry. Rehydrate in PBST for 5 min and cover with Abberior Mount Liquid Antifade. After sealing, the slices were placed at 4 ℃ overnight before imaging.

High-speed video microscopy

Cilia beating in the zebrafish pronephric duct was recorded at 4dpf as previously

described (Xie, Kang et al., 2020). To visualize sperm motility, adult male zebrafish were euthanized with ice-cold water. Excess water was removed from the fish's body, and the testes were carefully dissected using tweezers in cold Hank's solution (136.75 mM NaCl, 5.37 mM KCl, 0.25 mM Na_2HPO_4, 0.45mM KH_2PO_4, 1.3 mM CaCl2, 1 mM MgSO4, 4.17 mM $NaHCO_3$). The supernatant containing the sperm was carefully collected and placed on ice. A 6 μl aliquot of the supernatant was aspirated using a pipette and mixed with 2 μl of water. This mixture was then placed on top of a cover glass. The cover glass, with the sperm sample, was inverted and positioned in the center of a depression slide. Sperm motility was recorded using a 100X oil objective on a Leica Sp8 confocal microscope equipped with a high-speed camera (Motion-BLITZ EoSens mini1; Mikrotron, Germany), capturing images at a rate of 250 frames per second. Sperm movement trajectory was marked with manual tracking plugins in imageJ.

Statistical analysis

Statistical analysis was performed using GraphPad Prism 8 software. Student's t-test was used when the data follow a normal distribution, while the Mann-Whitney test was used when the data do not follow a normal distribution. Data for statistical analysis are expressed as mean ± s.d. unless otherwise stated. ImageJ software was used to measure length of cilia, fluorescence intensity and particle size.

Acknowledgments

We thank Dr. Guangshuo Ou and members of the Zhao lab for their kind help during the preparation of this manuscript. We are also grateful for the excellent support from the core facilities of IEMB at OUC. This work was supported by the National Natural Science Foundation of China (Nos. 32125015, 31991194 to C.Z. and No. 32100661 to H.X.) and the founding from Laoshan Laboratory (LSKJ202203204).

529 **Figures and legends**

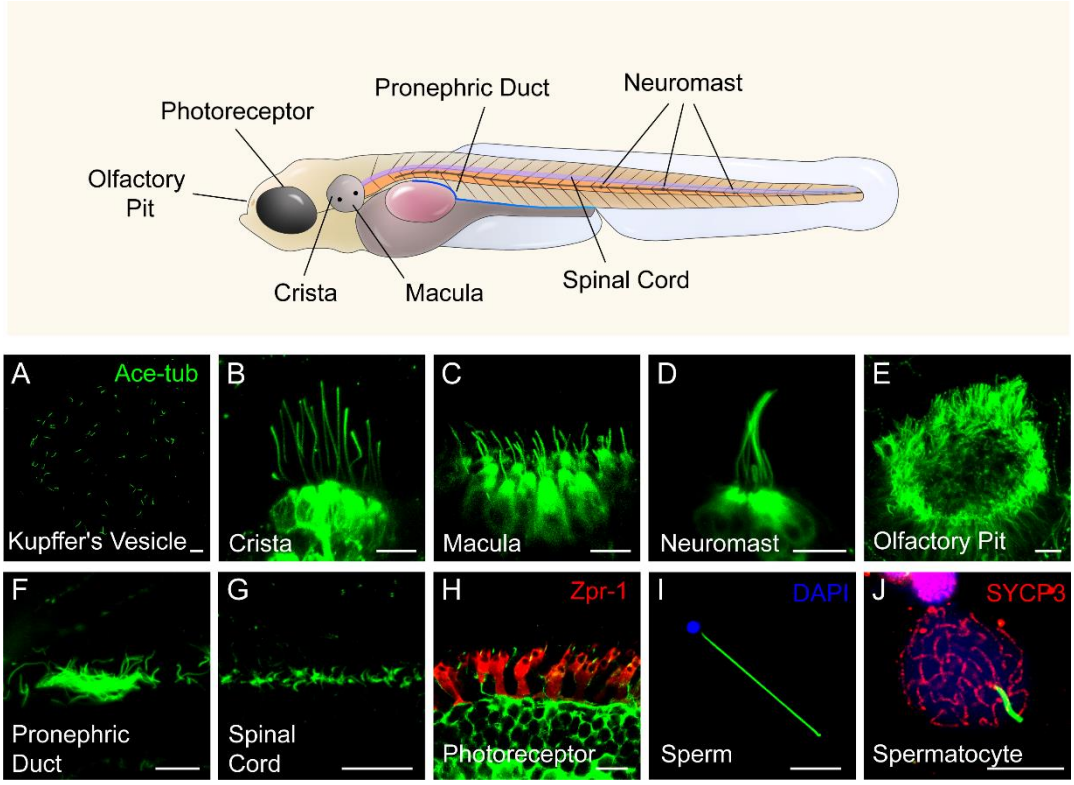

530

531 **Fig 1 Diverse type of cilia are present in zebrafish**

532 (A) Cilia in kupffer's vesicle (KV) of a 10-somite stage zebrafish larvae. (B-H) Confocal images
533 showing cilia in different type of cells at 4 dpf as indicated. The position of these cells were indicated
534 in the top diagram. (I-J) Confocal images showing cilia in the sperm (flagellum) or spermatocyte of
535 adult zebrafish. All the cilia were visualized with anti-acetyleated tubulin. The photoreceptor double
536 cones were stained with zpr-1 antibody in panel H, and nuclei were stained with DAPI in panel I.
537 Immunostaining with anti-SYCP3 labelled the synaptonemal complexes of primary spermatocytes
538 in panel J. Scale bar=10 μm.

539

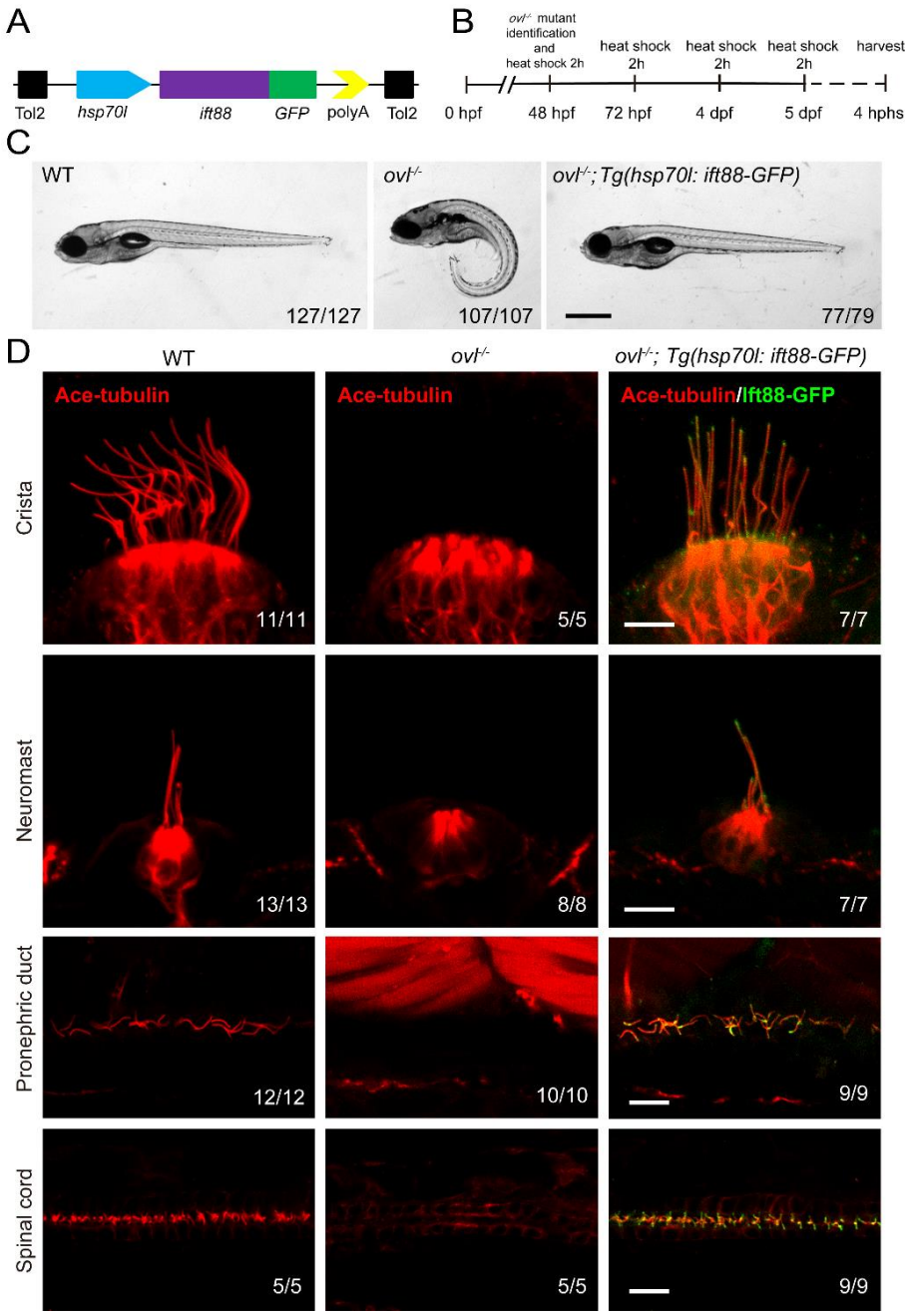

Fig 2 Rescue of *ovl* mutants with Tg(*hsp70l:ift88-GFP*) transgene.

(A) Schematic diagram of *hsp70l:ift88-GFP* construct. (B) Procedure of heat shock experiments for *ovl* mutants rescue assay. hphs, hour post heat shock. (C) External pheontype of 5 dpf wild type, *ovl* mutant or *ovl* mutant larvae carrying Tg(*hsp70l:ift88-GFP*) transgene. The numbers of larvae investigated were shown on the bottom right. (D) Confocal images showing cilia in different type of organs as indicated. Red channel indicates cilia visualized by anti-acetylated α-tubulin antibody and fluorescence of *Tg(hsp70l:ift88-GFP)* is showed in green. Scale bars: 200 μm in panel C and 10 μm in panel D.

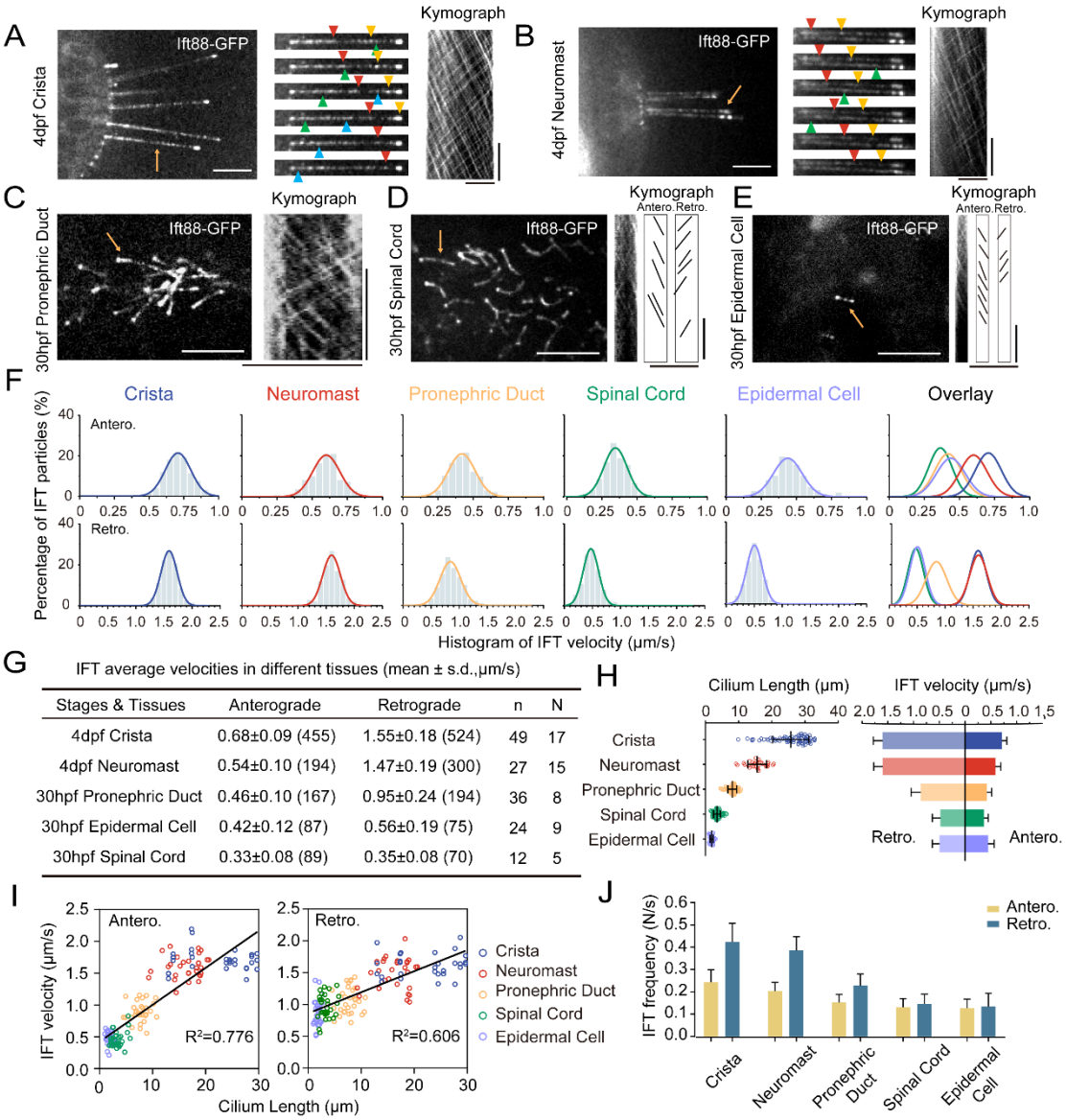

IFT average velocities in different tissues (mean ± s.d.,μm/s)

Stages & Tissues	Anterograde	Retrograde	n	N
4dpf Crista	0.68±0.09 (455)	1.55±0.18 (524)	49	17
4dpf Neuromast	0.54±0.10 (194)	1.47±0.19 (300)	27	15
30hpf Pronephric Duct	0.46±0.10 (167)	0.95±0.24 (194)	36	8
30hpf Epidermal Cell	0.42±0.12 (87)	0.56±0.19 (75)	24	9
30hpf Spinal Cord	0.33±0.08 (89)	0.35±0.08 (70)	12	5

Fig 3 Intraflagellar transport in different type of cilia.

(A-E) Left, Snapshot of Intraflagellar transport videos in different cell types as indicated. Middle (A, B), Snapshot of same cilia at different time points. Arrowheads with the same color indicate the same IFT particle. Right, kymographs illustrating the movement of IFT particles along the axoneme. Horizontal scale bar: 10 μm and vertical scale bars: 10 s. Representative particle traces are marked with black lines in panels D and E. Yellow arrows denote the cilia used to generating the kymograph. (F) Histograms displaying the velocity of anterograde and retrograde IFT in different type of cilia as indicated. “Antero.” and “Retro.” represent anterograde and retrograde transport, respectively. Each plot was fit by a Gaussian distribution. The developmental stages of zebrafish were consistent with (A-E) (G) Summary of IFT velocities in different tissues of zebrafish. Numbers of IFT particles

are shown in the brackets. n, number of cilia detected. N, number of zerafish larvae analyzed. hpf, hours post-fertilization. dpf, days post-fertilization. (H) Left, Statistics analysis of cilia length in different tissues of Tg(*hsp70l:ift88-GFP*) larvae (crista, n=72 cilia from 16 larvae; neuromast, n=31 cilia from 9 larvae; pronephric duct, n=72 cilia from 11 larvae; spinal cord, n=86 cilia from 6 larvae; epidermal cell, n=48 cilia from 18 larvae). Right, anterograde and retrograde IFT average velocity in different tissues of zebrafish. (I) Anterograde and retrograde IFT velocities plotted versus cilia length. Linear fit (black line) and coefficient of determination are indicated. (J) Frequency of anterograde and retrograde IFT entering or exiting cilia. (crista, n=47 cilia from 13 larvae; neuromast, n=31 cilia from 13 larvae; pronephric duct, n=43 cilia from 14 larvae; spinal cord, n=27 cilia from 7 larvae; epidermal cell, n=26 cilia from 15 larvae)

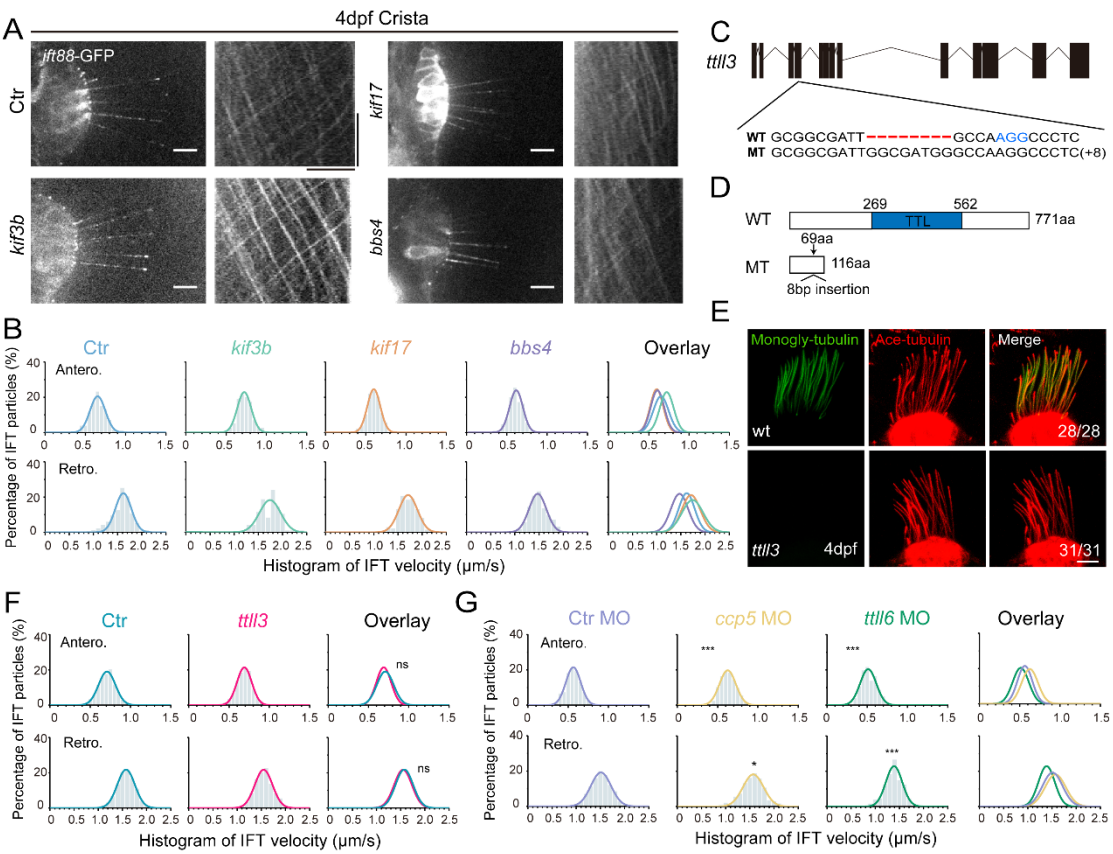

Fig 4 Alterations in motor proteins, BBSome proteins, or tubulin modifications have minimal effects on IFT.

(A) Left: Snapshot of IFT videos in crista cilia of 4dpf wild type or mutant larvae as indicated. Right: Kymographs showing IFT particle movement along axoneme visualized with Ift88:GFP. Horizontal scale bar: 10μm and vertical scale bar:10s. (B) Histograms showing anterograde and retrograde IFT velocity in crista cilia of control or mutant larvae. (C) Genomic structure and sequences of wild type and *ttll3* mutant allele. PAM sequence of sgRNA target are indicated in blue. (D) Protein domain of Ttll3 in wild type and *ttll3* mutants. (E) Confocal images showing crista cilia in 4dpf wild type (wt) or maternal-zygotic (MZ) *ttll3* mutant visualized with anti-monoglycylated tubulin antibody (green) and anti-acetylated α-tubulin antibody (red). (F) Histograms depicting IFT velocity in crista cilia of control and *ttll3* mutants. Top, anterograde IFT. Bottom, retrograde IFT.(G) Histograms illustrating IFT velocity in crista cilia of *ccp5* or *ttll6* morphants. Scale bars: 10 μm in panel A and 5 μm in panel E. *$p < 0.5$; *** $p < 0.001$. The average IFT velocity and the number of samples (N) are shown in Table 1.

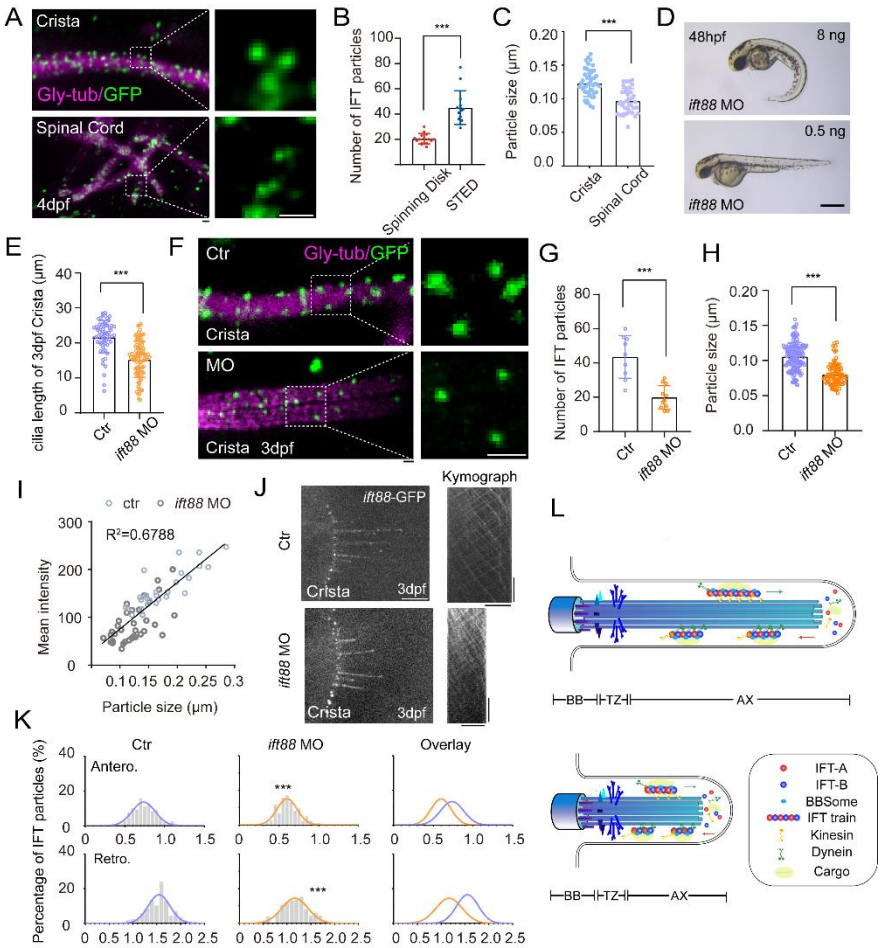

Fig 5 Increased size of IFT fluorescent particles in crista cilia.

(A) Representative STED images of crista (top) and spinal cord (bottom) in 4dpf *Tg(hsp70l: ift88-GFP)* larva. Cilia was stained with anti-monoglycylated tubulin (magenta), and IFT88-GFP particles were counterstained with anti-GFP antibody (green). Enlarged views of the boxed region are displayed on the right. (B) Dot plots showing the number of IFT particles per cilia in crista recorded by spinning disk and STED. (Spinning disk, n=15 cilia from 6 larvae; STED, n=14 cilia from 8 larvae.Two-tailed Mann-Whitney test) (C) Statistical analysis showing IFT particles size in the cilia of ear crista and spinal cord. (Crista, n=44 particles from 7 larvae; Spinal cord, n=35 particles from 5 larvae; Unpaired two-sided Student's t-test) (D) External phenotypes of 2 dpf zebrafish larvae injected with higher and lower dose of *ift88* morpholinos. (E) Cilia length quantification of control and *ift88* morphants. (ctr, n=62 cilia from 18 larvae; *ift88* MO, n=88 cilia from 17 larvae; Two-tailed Mann-Whitney test) (F) STED images showing IFT particles in crista cilia of 3dpf control or *ift88* morphants. Enlarged views of the boxed region are displayed on the right. (G) Dot plots showing the number of IFT particles per cilia in control and *ift88* morphants.

602 (ctr, n=9 cilia from 5 larvae; *ift88* MO, n=11 cilia from 6 larvae; Unpaired two-sided Student's t-
603 test) (H) Statistical analysis showing IFT particles size of crista cilia in control or *ift88* morphants.
604 (ctr, n=141 particles from 11 larvae; *ift88* MO, n=88 particles from 13 larvae; Two-tailed Mann-
605 Whitney test) (I) Mean intensity of IFT particles was plotted together with IFT particle size. Linear
606 fit (black line) and coefficient of determination are indicated. (J) Left, Snapshot of IFT videos in
607 crista cilia of 3dpf control (top) or *ift88* morphant (bottom) carrying *Tg(hsp70l: ift88-GFP)*. Right,
608 Kymographs showing movement of IFT particles along axoneme. Horizontal scale bar: 10 μm and
609 vertical scale bar:10s. (K) Histograms showing IFT velocity in the crista cilia of 3dpf control or
610 *ift88* morphants (Two-tailed Mann-Whitney test). (L) Model illustrating IFT with different train
611 sizes in long and short cilia. Scale bars: 0.2 μm in panel A and F, and 500 μm in panel I. ** $p < 0.01$;
612 *** $p < 0.001$. BB, basal body; TZ, transition zone; AX, axoneme.

613 **Supplementary figures**

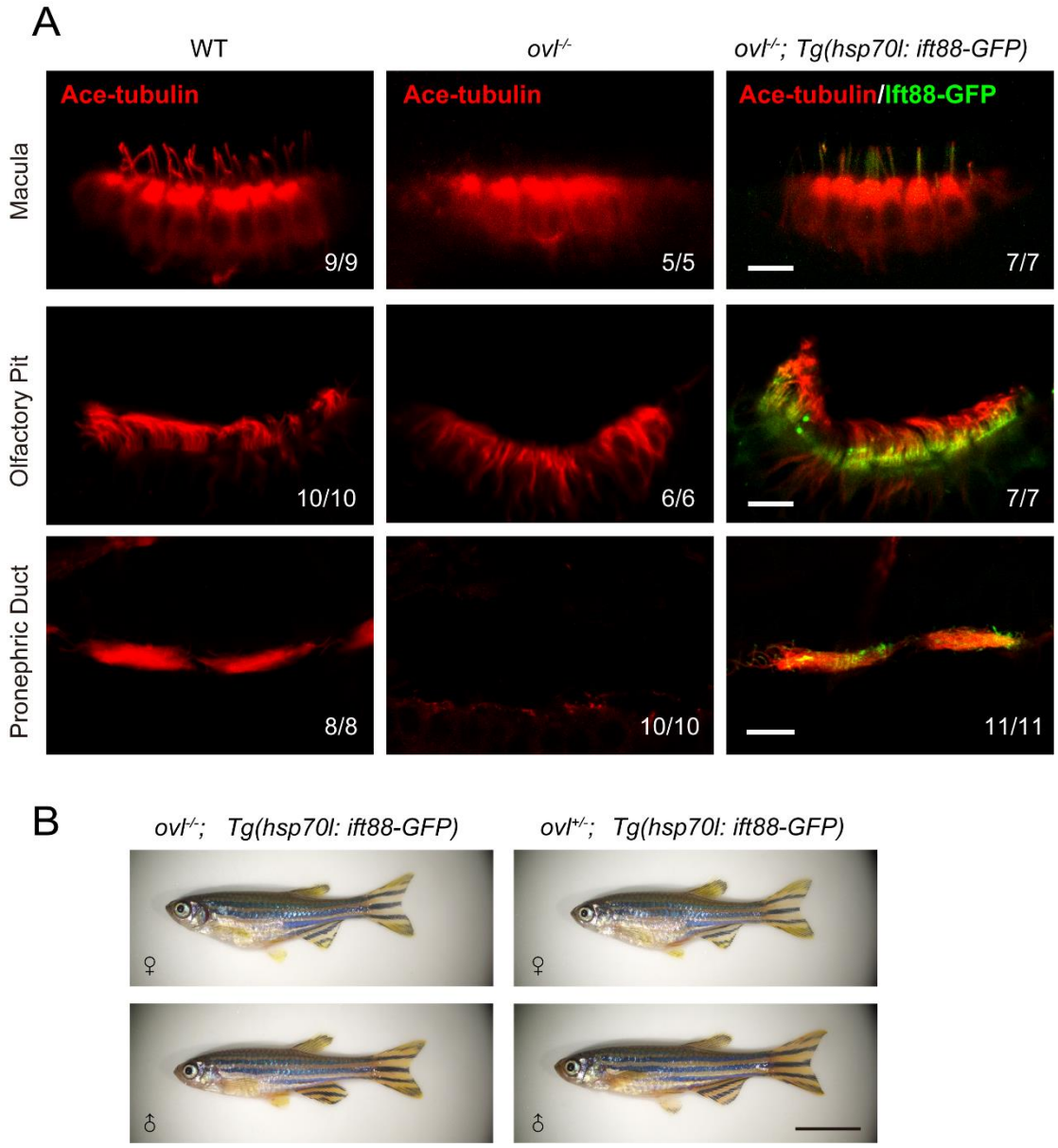

614

615 **Fig S1 Rescue of ciliogenesis defects in *ovl* (*ift88*) mutants via *Tg(hsp70l:ift88-GFP)***

616 (A) Rescue of ciliogenesis defects in ear macula, olfactory placode and pronephric duct. Red
617 channel shows cilia visualized by anti-acetylated α-tubulin antibody. Fluorescence of
618 *Tg(hsp70l:ift88-GFP)* is shown in green. (B) External phenotypes of adult *ovl* homozygotes rescued
619 with *Tg(hsp70l:ift88-GFP)* transgene. Scale bars:10 μm in panel A and 1cm in panel B.

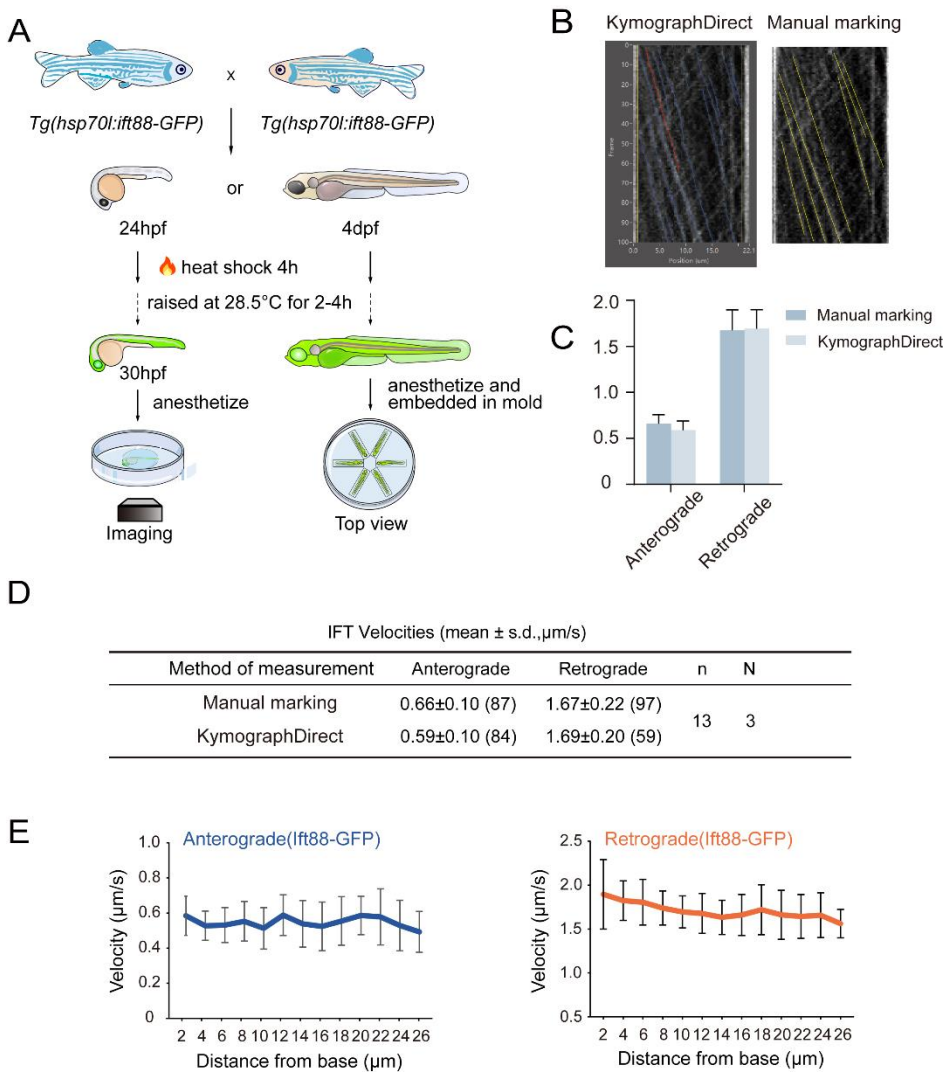

Fig S2 Overview of zebrafish larvae treatments and IFT velocity analysis

(A) Diagram showing the procedure of heat shock treatments of transgenic zebrafish larvae (see Methods for details). (B) Representative kymographs illustrating the movement of IFT particles along the axoneme using automated and manual marking methods. Left, lines represent trajectories fitted by KymographDirect. Right, particle traces are manually marked with lines. (C) Quantification of anterograde and retrograde average velocities in 4dpf crista cilia using two speed calculation methods. (D) Summary of anterograde and retrograde average velocities in 4dpf crista cilia using two speed calculation methods. Numbers of IFT particles are shown in the brackets. n, number of cilia. N, number of zerafish larvae. (E) Quantification of anterograde and retrograde velocities along the entire length of crista cilia. n=11 cilia from 15 larvae.

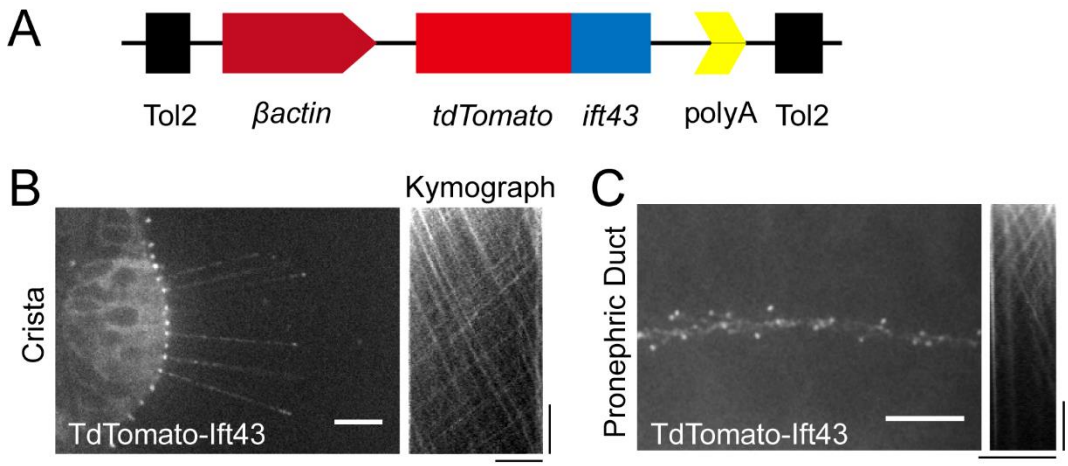

D

IFT Velocities (mean ± s.d.,μm/s)

Stages & Tissues	Anterograde	Retrograde	n	N
4dpf Crista	0.69±0.08 (160)	1.64±0.16 (180)	29	12
30hpf Pronephric Duct	0.39±0.09 (170)	0.78±0.16 (140)	54	8

Fig S3 Generation of Tg (*βactin*:*tdTomato-ift43*) transgene for IFT imaging

(A) Schematic diagram showing *βactin:tdTomato-ift43* transgenic construct. (B-C) Left, Snapshot of Intraflagellar transport videos in cilia of ear crista and pronephric duct epithelial cells. Right, kymographs illustrating the movement of IFT particles along the axoneme. Horizontal scale bar=10 μm. Vertical scale bar=10 s. (D) Summary of the anterograde and retrograde velocities of IFT measured in embryos expressing *Tg(βactin:tdTomato-ift43)*. Numbers of IFT particles are shown in the brackets. n, number of cilia. N, number of zerafish larvae.

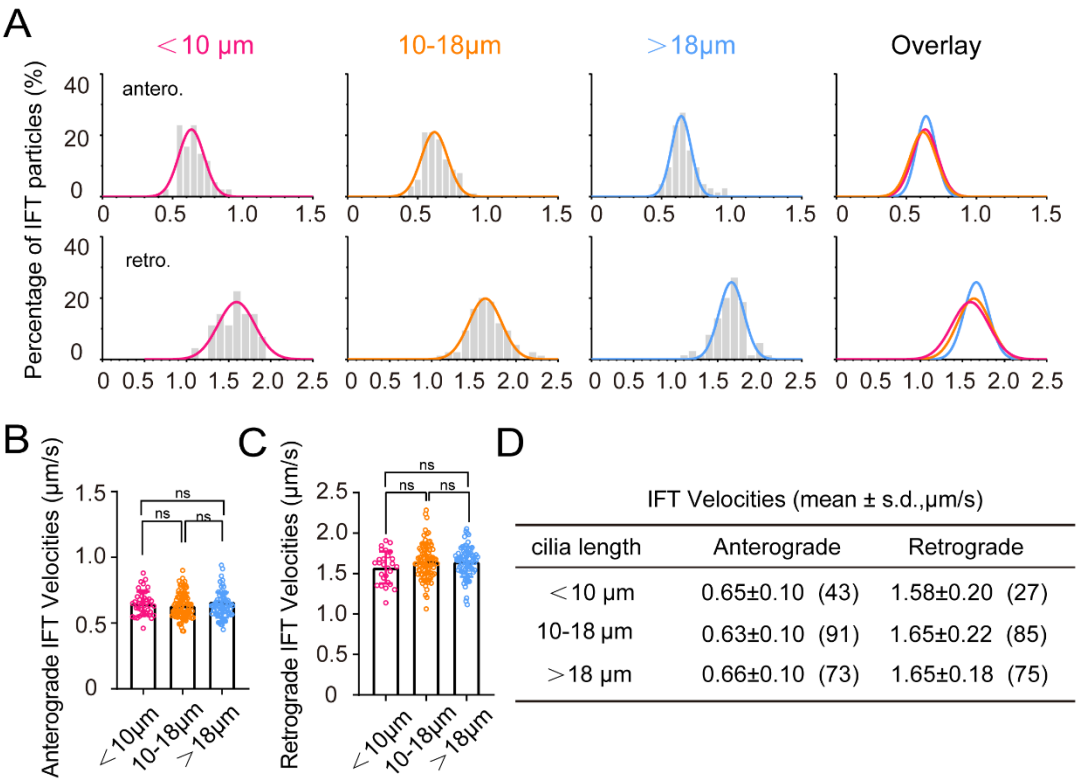

IFT Velocities (mean ± s.d.,μm/s)

cilia length	Anterograde	Retrograde
＜10 μm	0.65±0.10 (43)	1.58±0.20 (27)
10-18 μm	0.63±0.10 (91)	1.65±0.22 (85)
＞18 μm	0.66±0.10 (73)	1.65±0.18 (75)

Fig S4 IFT velocity in cilia of different lengths within crista.

(A) Histograms displaying the velocity of anterograde and retrograde IFT in crista cilia of different lengths as indicated. (B and C) Dot graphs showing the velocity of anterograde and retrograde IFT in crista cilia of different lengths. Statistical significance is based on one-way ANOVA, Bonferroni's multiple comparisons test. n.s., not significant, $p > 0.05$. (D) Summary of the anterograde and retrograde velocities in crista cilia of different lengths. Numbers of IFT particles are shown in the brackets. n=46 crista cilia from 14 4dpf larvae. < 10μm, n=12; 10-18μm, n=22, > 18μm, n=12.

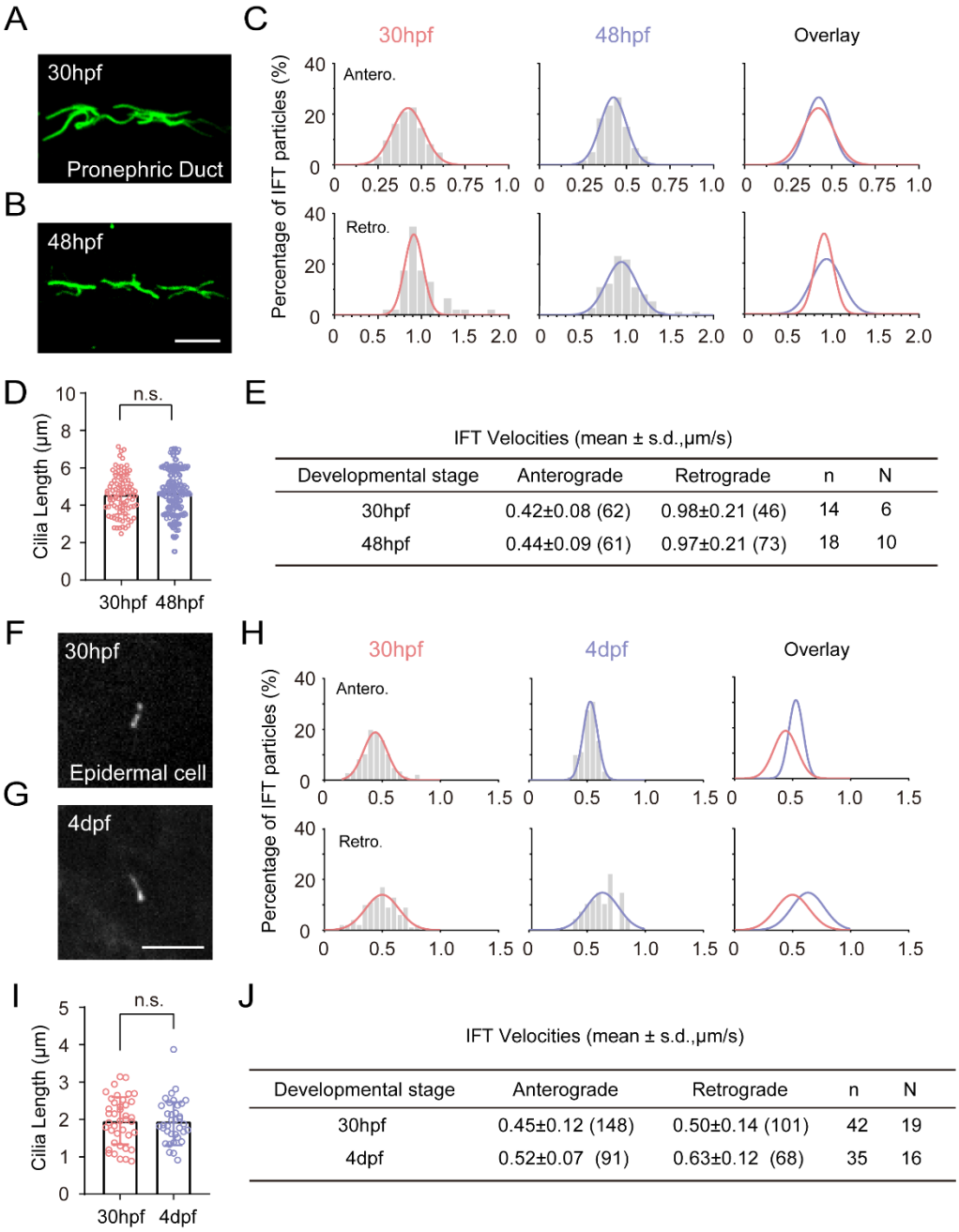

Fig S5 Comparison of cilia length and IFT volecity at different developmental stages

(A, B) Representative images showing cilia in the pronephric duct labeled with anti-acetylated tubulin in 30 hpf and 48 hpf zebrafish larvae. (C) Histograms displaying the velocity of anterograde and retrograde IFT in pronephric duct single cilia of 30 hpf and 48 hpf zebrafish larvae. (D) Length of pronephric duct single cilia of 30 hpf and 48 hpf zebrafish larvae (30 hpf, n=94; 48 hpf, n=97, Unpaired two-sided Student's t-test). (E) Summary of anterograde and retrograde average velocities in pronephric duct single cilia. (F, G) Snapshot of Tg*(hsp70l: ift88-GFP)* larvae IFT videos in epidermal cells of 30 hpf and 4 dpf zebrafish larvae. (H) Histograms

displaying the velocity of anterograde and retrograde IFT in epidermal cells cilia. (I) Length of epidermal cells cilia (30 hpf, n=40; 4 dpf, n=36, Unpaired two-sided Student's t-test) (J) Summary of anterograde and retrograde average velocities in epidermal cells cilia. "Antero." and "Retro." represent anterograde and retrograde transport, respectively. Each plot was fit by a Gaussian distribution. Scale bars=5 μm. Numbers of IFT particles are shown in the brackets. n, number of cilia. N, number of zerafish larvae. n.s., not significant, $p > 0.05$.

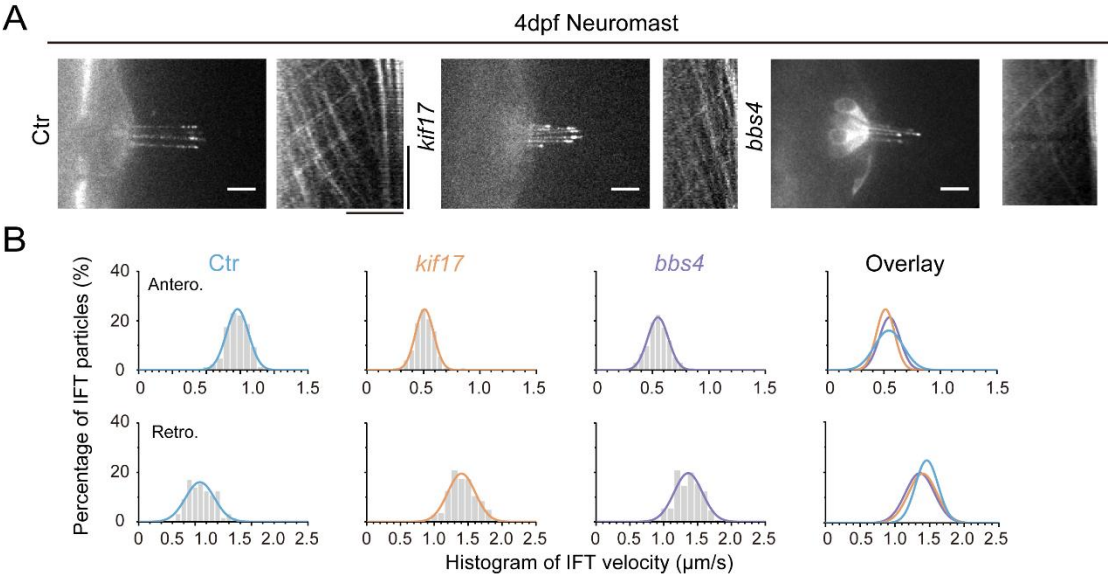

Fig S6 IFT in the cilia of neuromast hair cells of different zebrafish mutants.

(A)(Left) Snapshot of IFT videos in neuromast cilia of 4 dpf control, *kif17* or *bbs4* mutants. (Right) Kymographs showing IFT particle movement along axoneme. (B) Histograms showing anterograde and retrograde IFT velocity in neuromast cilia in control and mutants. Horizontal Scale bars=10μm. Vertical scale bar=10s.

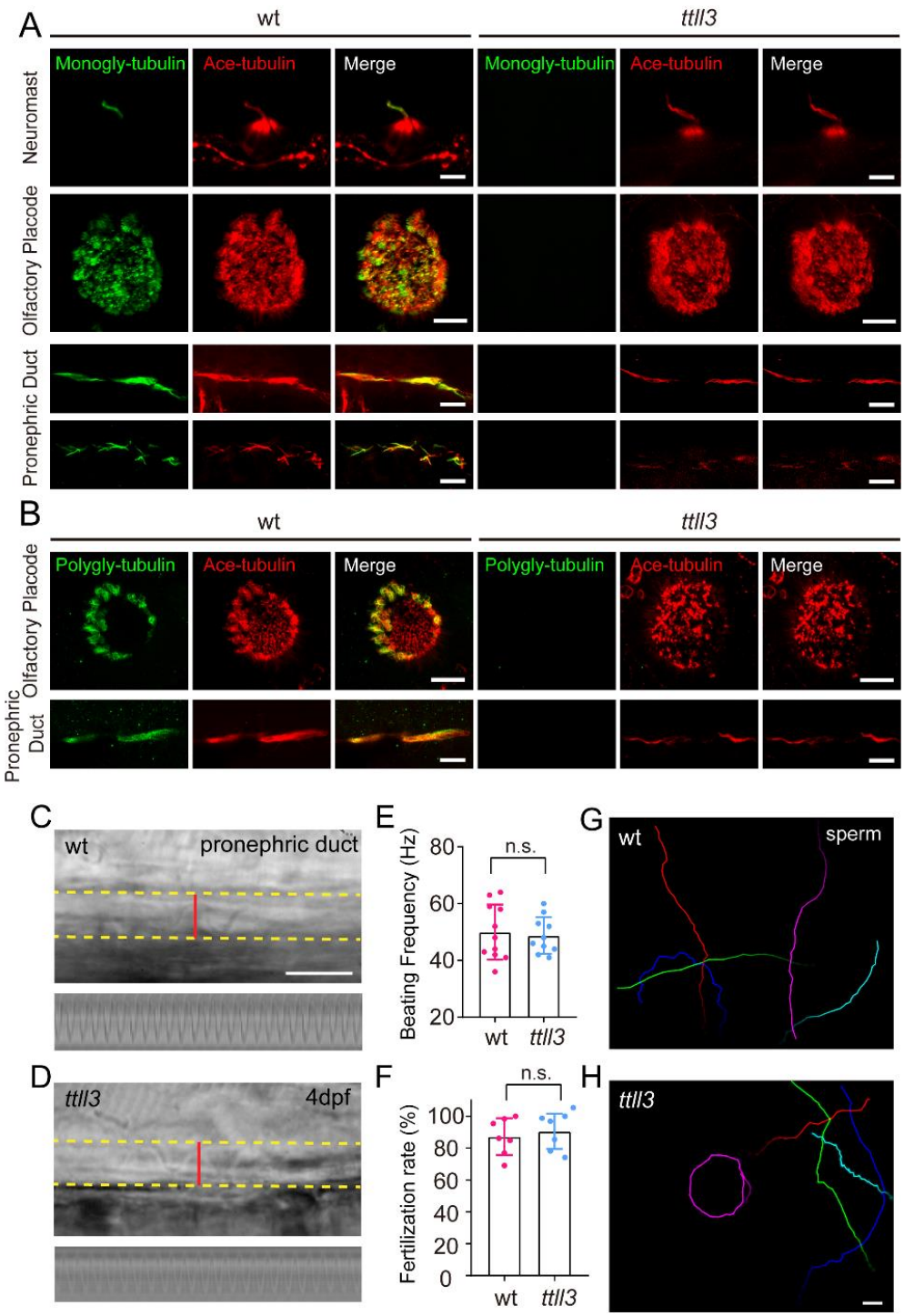

Fig S7 Loss of tubulin glycylation in *ttll3* mutants.

(A) Immunostaining with anti-monoglycylated tubulin antibody in 4 dpf *ttll3* mutants showing complete absence of monoglycylation modification in cilia of neuromast, olfactory placode and pronephric duct. (B) Immunostaining with anti-polyglycylated tubulin antibody revealed complete elimination of polyglycylation modification in multicilia of olfactory placode and pronephric duct. Red channel shows cilia visualized with anti-acetylated α-tubulin antibody. (C, D) Snapshots of

high-speed video showing cilia in pronephric duct of 5 dpf wild type (C) and *ttll3* (D) mutant. Bottom images show kymographs of cilia beating. The yellow dashed line indicates the boundary of pronephric duct, and the red line represents the path used to generate the kymograph. (E) Beating frequency of cilia in pronephric duct of wild type and *ttll3* mutant (wt, n=11; *ttll3*, n=10, Unpaired two-sided Student's t-test). (F) Statistical results showing fertilization rate of wild type and *ttll3* mutant (n=7, Unpaired two-sided Student's t-test). (G, H) Sperm movement trajectory of wild type (G) and *ttll3* (H) mutant within 2 seconds. Scale bar=5 μm in panel A and B, and 10μm in panel C, D, G and H.

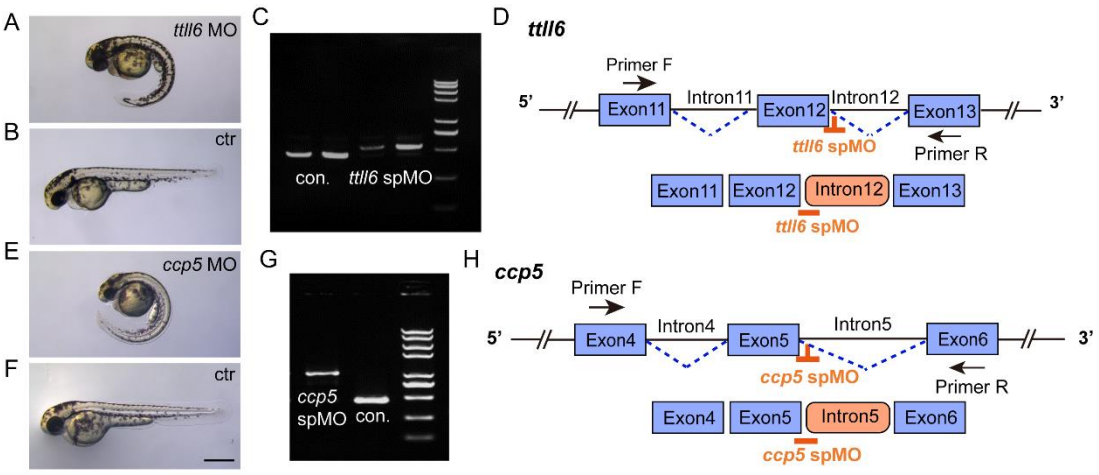

Fig S8 Validation of the efficiency of *ttll6* and *ccp5* morpholinos.

(A, B, E ,F) External phenotypes of control, *ttll6* and *ccp5* morphant embryos at 2 dpf. (C) Agarose gel electrophoresis of RT-PCR amplicons using primer pairs as indicated in panel (D). The PCR product size in the *ttll6* morphants was significantly larger than that in the control (con.). (D) Schematic diagram of *ttll6* sp MO target sites (orange) and RT-PCR primer positions. Sequencing results indicated that *ttll6* morphant exhibited incorrect splicing, with intron12 being incorrectly included in the mature mRNA. (G) Agarose gel analysis of RT-PCR amplicons using primer pairs as indicated in panel (H). The PCR product size in the *ccp5* morphant was significantly larger than that in the control (con.). (H)Schematic diagram illustrating the splice donor sites targeted by antisense morpholinos (orange). Injection of *ccp5* MO resulted in the production of aberrant transcripts, wherein intron 5 was mis-spliced into the mature mRNA. Scale bar =500 μm.

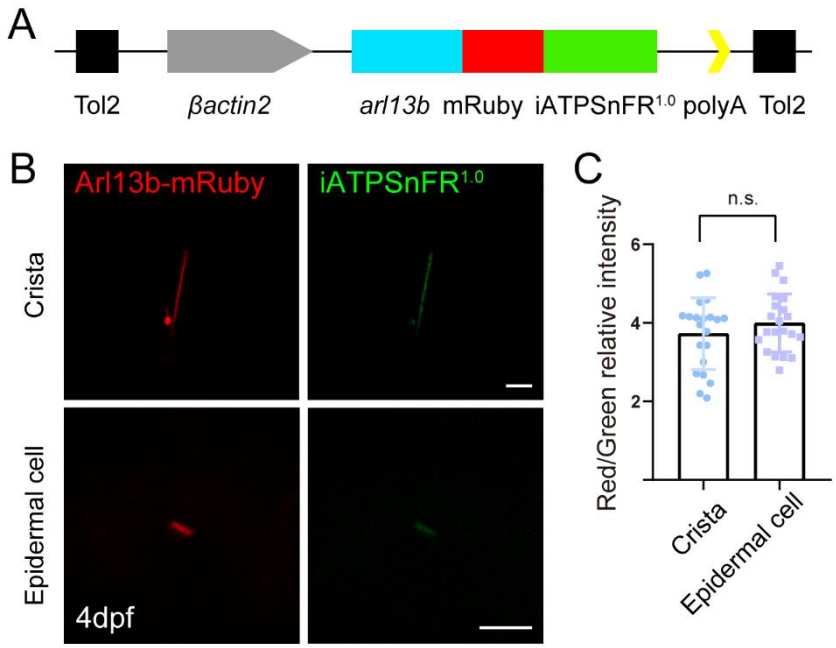

Fig S9 Generation of ATP reporter transgenic line.

(A) Schematic diagram of *βactin: arl13b-mRuby-iATPSnFR1.0* transgenic construct. (B) Confocal images showing cilia of crista and epidermal cell in 4dpf transgenic embryos. (C) Statistical results of relative fluorescence intensity (ratio of red fluorescence intensity vs green fluorescence intensity) in cilia of crista and epidermal cells (crista, n=22 cilia from 17 larvae; epidermal cell, n=21 cilia from 13 larvae. Mann-Whitney test. n.s., not significant, $p > 0.05$). Scale bar=5μm.

Table S1

IFT average velocities in ear crista cilia of control or mutant larvae. (mean ± s.d.,μm/s)

	Anterograde	Retrograde	n	N
ctr	0.65±0.10(182)	1.58±0.21(168)	28	12
kif3b	0.73±0.09(115)	1.74±0.22(96)	16	9
kif17	0.60±0.08(127)	1.72±0.18(136)	25	12
bbs4	0.61±0.08(110)	1.49±0.19(125)	14	10

IFT average velocities in neuromast cilia of control or mutant larvae. (mean ± s.d.,μm/s)

	Anterograde	Retrograde	n	N
ctr	0.56±0.12(66)	1.46±0.15(87)	11	6
kif17	0.52±0.08(127)	1.42±0.20(144)	26	13
bbs4	0.55±0.09(134)	1.36±0.19(130)	24	12

IFT average velocities in larvae injected ctr MO, *ccp5* MO and *ttll6* MO.(mean ± s.d.,μm/s)

	Anterograde	Retrograde	n	N
ctr MO	0.56±0.09(287)	1.51±0.20(256)	30	10
ccp5 MO	0.63±0.10(256)	1.56±0.23(234)	27	11
ttll6 MO	0.52±0.09(305)	1.38±0.18(305)	45	16

IFT average velocities in crista cilia of control and *ttll3* mutant larvae. (mean ± s.d.,μm/s)

	Anterograde	Retrograde	n	N
ctr	0.71±0.10(489)	1.57±0.19(549)	53	20
ttll3	0.69±0.09(481)	1.56±0.18(553)	56	22

IFT average velocities in larvae injected ctr MO and low dose *ift88* MO.(mean ± s.d.,μm/s)

	Anterograde	Retrograde	n	N
ctr MO	0.74±0.23(108)	1.55±0.27(118)	24	9
ift88 MO	0.62±0.14(158)	1.18±0.27(182)	38	13

Numbers of IFT particles are shown in the brackets. n, number of cilia. N, number of zerafish larvae.

Table S1 Summary of average IFT velocities in different zebrafish muants or morphants.

710 **Supplementary Videos**

711 Time-lapse images were continuously collected at an exposure time of 200 ms. The display rate was

712 20 frames per second. Scale bar: 10 μm. The elapsed time is displayed in the top left corner.

713 **Video 1：** Fluorescence time-lapse movie of ear crista cilia visualized by *Tg(hsp70l: ift88-GFP)*.

714 **Video 2：** Fluorescence time-lapse movie of neuromast cilia visualized by *Tg(hsp70l: ift88-GFP)*.

715 **Video 3：** Fluorescence time-lapse movie of pronephric duct cilia visualized by *Tg(hsp70l: ift88-*

716 *GFP)*.

717 **Video 4：** Fluorescence time-lapse movie of spinal cord cilia visualized by *Tg(hsp70l: ift88-GFP).*

718 **Video 5：** Fluorescence time-lapse movie of skin epidermal cells cilia visualized by *Tg(hsp70l:*

719 *ift88-GFP).*

720 **Video 6-9：** Fluorescence time-lapse movies of ear crista cilia in *kif17*, *kif3b*, *bbs4* and *ttll3*

721 mutants visualized by *Tg(hsp70l: ift88-GFP)*.

722 **Video 10：** Fluorescence time-lapse movies of ear crista cilia in *Tg(hsp70l: ift88-GFP)* embryos

723 injected with lower dose of *ift88* morpholinos.

724

REFERENCES

Berbari NF, Lewis JS, Bishop GA, Askwith CC, Mykytyn K (2008) Bardet-Biedl syndrome proteins are required for the localization of G protein-coupled receptors to primary cilia. *Proc Natl Acad Sci U S A* 105: 4242-6

Bhogaraju S, Cajanek L, Fort C, Blisnick T, Weber K, Taschner M, Mizuno N, Lamla S, Bastin P, Nigg EA, Lorentzen E (2013) Molecular basis of tubulin transport within the cilium by IFT74 and IFT81. *Science* 341: 1009-12

Chan YH, Marshall WF (2012) How cells know the size of their organelles. *Science* 337: 1186-9

Engel BD, Ludington WB, Marshall WF (2009) Intraflagellar transport particle size scales inversely with flagellar length: revisiting the balance-point length control model. *J Cell Biol* 187: 81-9

Gadadhar S, Alvarez Viar G, Hansen JN, Gong A, Kostarev A, Ialy-Radio C, Leboucher S, Whitfield M, Ziyyat A, Toure A, Alvarez L, Pigino G, Janke C (2021) Tubulin glycylation controls axonemal dynein activity, flagellar beat, and male fertility. *Science* 371

Goetz SC, Anderson KV (2010) The primary cilium: a signalling centre during vertebrate development. *Nat Rev Genet* 11: 331-44

Han YM, Kang GM, Byun K, Ko HW, Kim J, Shin MS, Kim HK, Gil SY, Yu JH, Lee B, Kim MS (2014) Leptin-promoted cilia assembly is critical for normal energy balance. *J Clin Invest* 124: 2193-7

Hesketh SJ, Mukhopadhyay AG, Nakamura D, Toropova K, Roberts AJ (2022) IFT-A structure reveals carriages for membrane protein transport into cilia. *Cell* 185: 4971-4985 e16

Hong SR, Wang CL, Huang YS, Chang YC, Chang YC, Pusapati GV, Lin CY, Hsu N, Cheng HC, Chiang YC, Huang WE, Shaner NC, Rohatgi R, Inoue T, Lin YC (2018) Spatiotemporal manipulation of ciliary glutamylation reveals its roles in intraciliary trafficking and Hedgehog signaling. *Nat Commun* 9: 1732

Iomini C, Babaev-Khaimov V, Sassaroli M, Piperno G (2001) Protein particles in Chlamydomonas flagella undergo a transport cycle consisting of four phases. *J Cell Biol* 153: 13-24

Ishikawa H, Moore J, Diener DR, Delling M, Marshall WF (2023) Testing the ion-current model for flagellar length sensing and IFT regulation. *Elife* 12

Janke C, Bulinski JC (2011) Post-translational regulation of the microtubule cytoskeleton: mechanisms and functions. *Nat Rev Mol Cell Biol* 12: 773-86

Jin H, White SR, Shida T, Schulz S, Aguiar M, Gygi SP, Bazan JF, Nachury MV (2010) The conserved Bardet-Biedl syndrome proteins assemble a coat that traffics membrane proteins to cilia. *Cell* 141: 1208-19

Jordan MA, Diener DR, Stepanek L, Pigino G (2018) The cryo-EM structure of intraflagellar transport trains reveals how dynein is inactivated to ensure unidirectional anterograde movement in cilia. *Nat Cell Biol* 20: 1250-1255

Kardon JR, Vale RD (2009) Regulators of the cytoplasmic dynein motor. *Nature Reviews Molecular Cell Biology* 10: 854

Kozminski KG, Beech PL, Rosenbaum JL (1995) The Chlamydomonas kinesin-like protein FLA10 is involved in motility associated with the flagellar membrane. *J Cell Biol* 131: 1517-27

Kozminski KG, Johnson KA, Forscher P, Rosenbaum JL (1993) A motility in the eukaryotic flagellum unrelated to flagellar beating. *Proceedings of the National Academy of Sciences* 90: 5519-5523

Kwan KM, Fujimoto E, Grabher C, Mangum BD, Hardy ME, Campbell DS, Parant JM, Yost HJ, Kanki JP, Chien CB (2007) The Tol2kit: A multisite gateway-based construction kit for Tol2 transposon transgenesis constructs. *Developmental Dynamics*

Lechtreck KF, Johnson EC, Sakai T, Cochran D, Ballif BA, Rush J, Pazour GJ, Ikebe M, Witman GB (2009) The Chlamydomonas reinhardtii BBSome is an IFT cargo required for export of specific signaling proteins from flagella. *J Cell Biol* 187: 1117-32

Leventea E, Hazime K, Zhao C, Malicki J (2016) Analysis of cilia structure and function in zebrafish. *Methods Cell Biol* 133: 179-227

Li S, Wan KY, Chen W, Tao H, Liang X, Pan J (2020) Functional exploration of heterotrimeric kinesin-II in IFT and ciliary length control in Chlamydomonas. *Elife* 9

Li X, Yang S, Deepak V, Chinipardaz Z, Yang S (2021) Identification of Cilia in Different Mouse Tissues. *Cells* 10

Liu J, Xie H, Wu M, Hu Y, Kang Y (2023) The role of cilia during organogenesis in zebrafish. *Open Biol* 13: 230228

Liu YX, Xue B, Sun WY, Wingfield JL, Sun J, Wu M, Lechtreck KF, Wu Z, Fan ZC (2021) Bardet-Biedl syndrome 3 protein promotes ciliary exit of the signaling protein phospholipase D via the BBSome. *Elife* 10

Lobas MA, Tao R, Nagai J, Kronschlager MT, Borden PM, Marvin JS, Looger LL, Khakh BS (2019) A genetically encoded single-wavelength sensor for imaging cytosolic and cell surface ATP. *Nat Commun* 10: 711

Ludington WB, Wemmer KA, Lechtreck KF, Witman GB, Marshall WF (2013) Avalanche-like behavior in ciliary import. *Proc Natl Acad Sci U S A* 110: 3925-30

Mangeol P, Prevo B, Peterman EJ (2016) KymographClear and KymographDirect: two tools for the automated quantitative analysis of molecular and cellular dynamics using kymographs. *Mol Biol Cell* 27: 1948-57

Marshall WF (2023) The flagellar length control system: exploring the physical biology of organelle size. *Phys Biol* 20

Meleppattu S, Zhou H, Dai J, Gui M, Brown A (2022) Mechanism of IFT-A polymerization into trains for ciliary transport. *Cell* 185: 4986-4998 e12

Mill P, Christensen ST, Pedersen LB (2023) Primary cilia as dynamic and diverse signalling hubs in development and disease. *Nat Rev Genet* 24: 421-441

Nachury MV, Loktev AV, Zhang Q, Westlake CJ, Peranen J, Merdes A, Slusarski DC, Scheller RH, Bazan JF, Sheffield VC, Jackson PK (2007) A core complex of BBS proteins cooperates with the GTPase Rab8 to promote ciliary membrane biogenesis. *Cell* 129: 1201-13

Nachury MV, Mick DU (2019) Establishing and regulating the composition of cilia for signal transduction. *Nat Rev Mol Cell Biol* 20: 389-405

O'Hagan R, Silva M, Nguyen KCQ, Zhang W, Bellotti S, Ramadan YH, Hall DH, Barr MM (2017) Glutamylation Regulates Transport, Specializes Function, and Sculpts the Structure of Cilia. *Curr Biol* 27: 3430-3441 e6

Ogino T, Sawada M, Takase H, Nakai C, Herranz-Pérez V, Cebrián-Silla A, Kaneko N, García-Verdugo JM, Sawamoto K (2016) Characterization of multiciliated ependymal cells that emerge in the neurogenic niche of the aged zebrafish brain. *Journal of Comparative Neurology* 524: 2982-2992

Orozco JT, Wedaman KP, Signor D, Brown H, Rose L, Scholey JM (1999) Movement of motor and cargo along cilia. *Nature* 398: 674

Ou G, Blacque OE, Snow JJ, Leroux MR, Scholey JM (2005) Functional coordination of intraflagellar transport motors. *Nature* 436: 583-587

Ou G, Koga M, Blacque OE, Murayama T, Ohshima Y, Schafer JC, Li C, Yoder BK, Leroux MR, Scholey JM (2007) Sensory ciliogenesis in Caenorhabditis elegans: assignment of IFT components into distinct modules based on transport and phenotypic profiles. *Mol Biol Cell* 18: 1554-69

Pathak N, Austin-Tse CA, Liu Y, Vasilyev A, Drummond IA (2014) Cytoplasmic carboxypeptidase 5 regulates tubulin glutamylation and zebrafish cilia formation and function. *Mol Biol Cell* 25: 1836-44

Pathak N, Austin CA, Drummond IA (2011) Tubulin tyrosine ligase-like genes ttll3 and ttll6 maintain zebrafish cilia structure and motility. *J Biol Chem* 286: 11685-95

Penny GM, Dutcher SK (2024) Gene dosage of independent dynein arm motor preassembly factors influences cilia assembly in Chlamydomonas reinhardtii. *PLoS Genet* 20: e1011038

Reiter JF, Leroux MR (2017) Genes and molecular pathways underpinning ciliopathies. *Nat Rev Mol Cell Biol* 18: 533-547

Rosenbaum JL, Moulder JE, Ringo DL (1969) Flagellar elongation and shortening in Chlamydomonas. The use of cycloheximide and colchicine to study the synthesis and assembly of flagellar proteins. *J Cell Biol* 41: 600-19

Scholey, J. M (2008) Intraflagellar transport motors in cilia: moving along the cell's antenna. *The Journal of Cell Biology* 180: 23-29

Signor D, Wedaman KP, Orozco JT, Dwyer ND, Bargmann CI, Rose LS, Scholey JM (1999) Role of a class DHC1b dynein in retrograde transport of IFT motors and IFT raft particles along cilia, but not dendrites, in chemosensory neurons of living Caenorhabditis elegans. *J Cell Biol* 147: 519-30

Singla V, Reiter JF (2006) The primary cilium as the cell's antenna: signaling at a sensory organelle. *Science* 313: 629-33

Sirajuddin M, Rice LM, Vale RD (2014) Regulation of microtubule motors by tubulin isotypes and post-translational modifications. *Nat Cell Biol* 16: 335-44

Snow JJ, Ou G, Gunnarson AL, Walker MR, Zhou HM, Brust-Mascher I, Scholey JM (2004) Two anterograde intraflagellar transport motors cooperate to build sensory cilia on C. elegans neurons. *Nat Cell Biol* 6: 1109-13

Song Z, Zhang X, Jia S, Yelick PC, Zhao C (2016) Zebrafish as a Model for Human Ciliopathies. *Journal of Genetics & Genomics* 43: 107-120

Stepanek L, Pigino G (2016) Microtubule doublets are double-track railways for intraflagellar transport trains. *Science* 352: 721-4

Stukalin EB, Phillips H, 3rd, Kolomeisky AB (2005) Coupling of two motor proteins: a new motor can move faster. *Phys Rev Lett* 94: 238101

Taschner M, Bhogaraju S, Lorentzen E (2012) Architecture and function of IFT complex proteins in ciliogenesis. *Differentiation* 83: S12-S22

Tsang SH, Aycinena ARP, Sharma T (2018) Ciliopathy: Bardet-Biedl Syndrome. *Adv Exp Med Biol* 1085: 171-174

Tsujikawa M, Malicki J (2004a) Intraflagellar Transport Genes Are Essential for Differentiation and Survival of Vertebrate Sensory Neurons. *Neuron* 42: 703-716

Tsujikawa M, Malicki J (2004b) Intraflagellar transport genes are essential for differentiation and survival of vertebrate sensory neurons. *Neuron* 42: 703-16

Tu HQ, Li S, Xu YL, Zhang YC, Li PY, Liang LY, Song GP, Jian XX, Wu M, Song ZQ, Li TT, Hu HB, Yuan JF, Shen XL, Li JN, Han QY, Wang K, Zhang T, Zhou T, Li AL et al. (2023) Rhythmic cilia changes support SCN neuron coherence in circadian clock. *Science* 380: 972-979

Urnavicius L, Lau CK, Elshenawy MM, Morales-Rios E, Motz C, Yildiz A, Carter AP (2018) Cryo-EM shows how dynactin recruits two dyneins for faster movement. *Nature* 554: 202-206

Uytingco CR, Williams CL, Xie C, Shively DT, Green WW, Ukhanov K, Zhang L, Nishimura DY, Sheffield VC, Martens JR (2019) BBS4 is required for intraflagellar transport coordination and basal body number in mammalian olfactory cilia. *J Cell Sci* 132

Vannuccini E, Paccagnini E, Cantele F, Gentile M, Dini D, Fino F, Diener D, Mencarelli C, Lupetti P (2016) Two classes of short intraflagellar transport train with different 3D structures are present in Chlamydomonas flagella. *J Cell Sci* 129: 2064-74

Visscher K, Schnitzer MJ, Block SM (1999) Single kinesin molecules studied with a molecular force clamp. *Nature* 400: 184-9

Wemmer K, Ludington W, Marshall WF (2020) Testing the role of intraflagellar transport in flagellar length control using length-altering mutants of Chlamydomonas. *Philos Trans R Soc Lond B Biol Sci* 375: 20190159

Williams CL, McIntyre JC, Norris SR, Jenkins PM, Zhang L, Pei Q, Verhey K, Martens JR (2014) Direct evidence for BBSome-associated intraflagellar transport reveals distinct properties of native mammalian cilia. *Nat Commun* 5: 5813

Wloga D, Webster DM, Rogowski K, Bre MH, Levilliers N, Jerka-Dziadosz M, Janke C, Dougan ST, Gaertig J (2009) TTLL3 Is a tubulin glycine ligase that regulates the assembly of cilia. *Dev Cell* 16: 867-76

Xie H, Kang Y, Wang S, Zheng P, Chen Z, Roy S, Zhao C (2020) E2f5 is a versatile transcriptional activator required for spermatogenesis and multiciliated cell differentiation in zebrafish. *PLoS Genet* 16: e1008655

Ye F, Nager AR, Nachury MV (2018) BBSome trains remove activated GPCRs from cilia by enabling passage through the transition zone. *J Cell Biol* 217: 1847-1868

Yi P, Li WJ, Dong MQ, Ou G (2017) Dynein-Driven Retrograde Intraflagellar Transport Is Triphasic in C. elegans Sensory Cilia. *Curr Biol* 27: 1448-1461 e7

Zhao C, Omori Y, Brodowska K, Kovach P, Malicki J (2012) Kinesin-2 family in vertebrate ciliogenesis. *Proceedings of the National Academy of Sciences* 109: 2388 - 2393

Zhou HM, Brust-Mascher I, Scholey JM (2001) Direct visualization of the movement of the monomeric axonal transport motor UNC-104 along neuronal processes in living Caenorhabditis elegans. *J Neurosci* 21: 3749-55

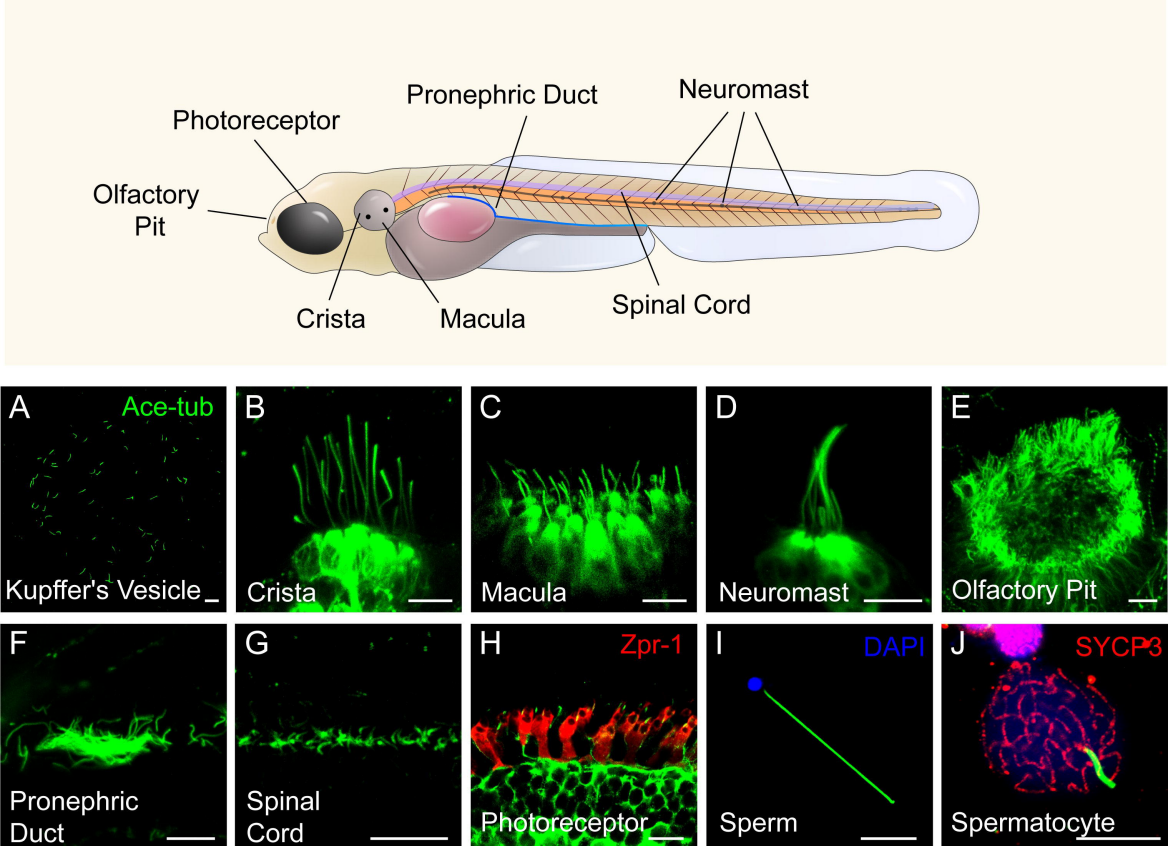
Photoreceptor
Pronephric Duct
Neuromast
Olfactory Pit
Crista
Macula
Spinal Cord
A
Ace-tub
Kupffer's Vesicle
B
Crista
C
Macula
D
Neuromast
E
Olfactory Pit
F
Pronephric Duct
G
Spinal Cord
H
Zpr-1
Photoreceptor
I
DAPI
Sperm
J
SYCP3
Spermatocyte

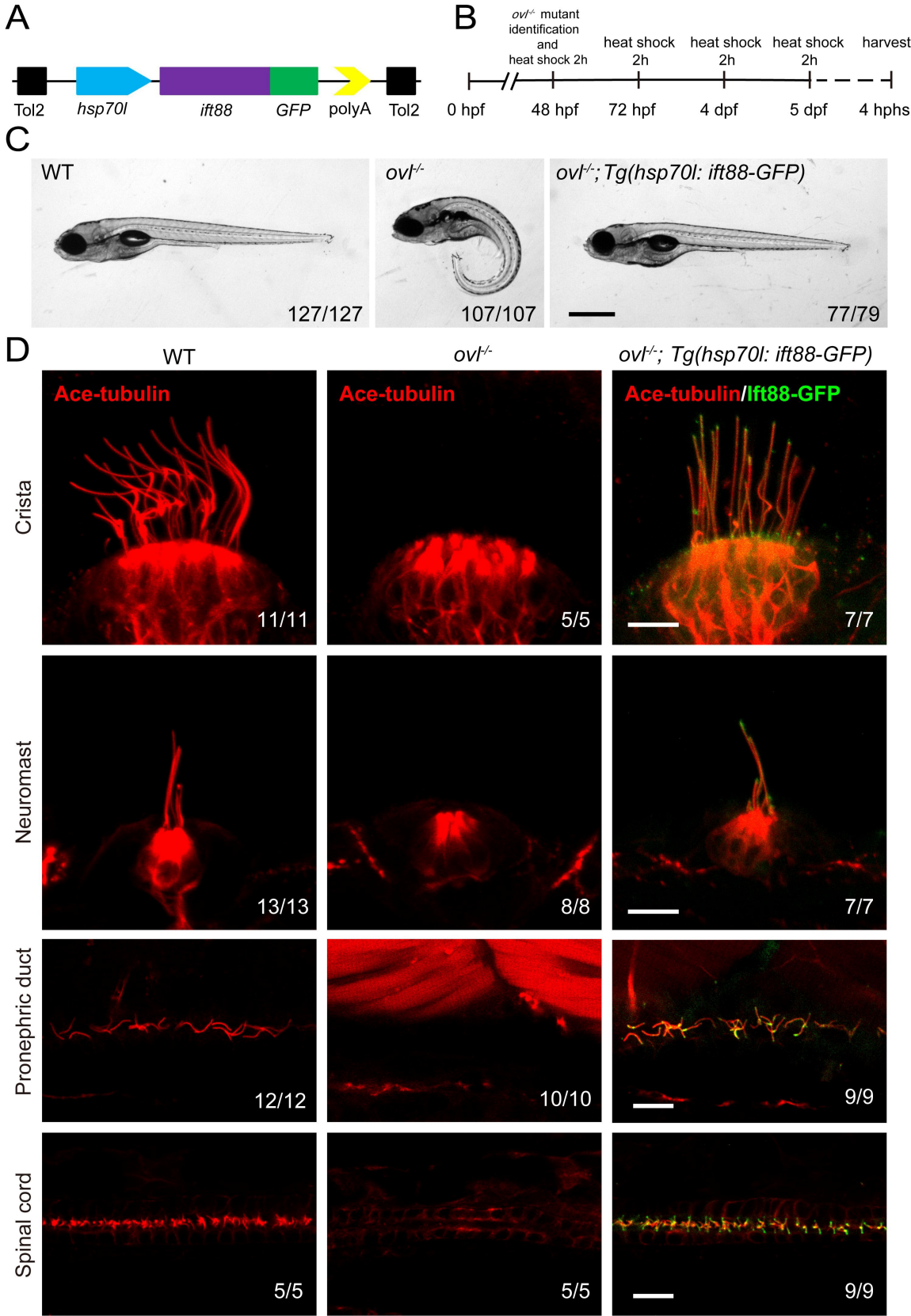
A
Tol2
hsp70l
ift88
GFP
polyA
Tol2
B
ovl-/- mutant identification and heat shock 2h
heat shock 2h
heat shock 2h
heat shock 2h
harvest
0 hpf
48 hpf
72 hpf
4 dpf
5 dpf
4 hphs
C
WT
127/127
ovl-/-
107/107
ovl-/-; Tg(hsp70l: ift88-GFP)
77/79
D
WT
ovl-/-
ovl-/-; Tg(hsp70l: ift88-GFP)
Crista
Ace-tubulin
11/11
Ace-tubulin
5/5
Ace-tubulin/Ift88-GFP
7/7
Neuromast
13/13
8/8
7/7
Pronephric duct
12/12
10/10
9/9
Spinal cord
5/5
5/5
9/9

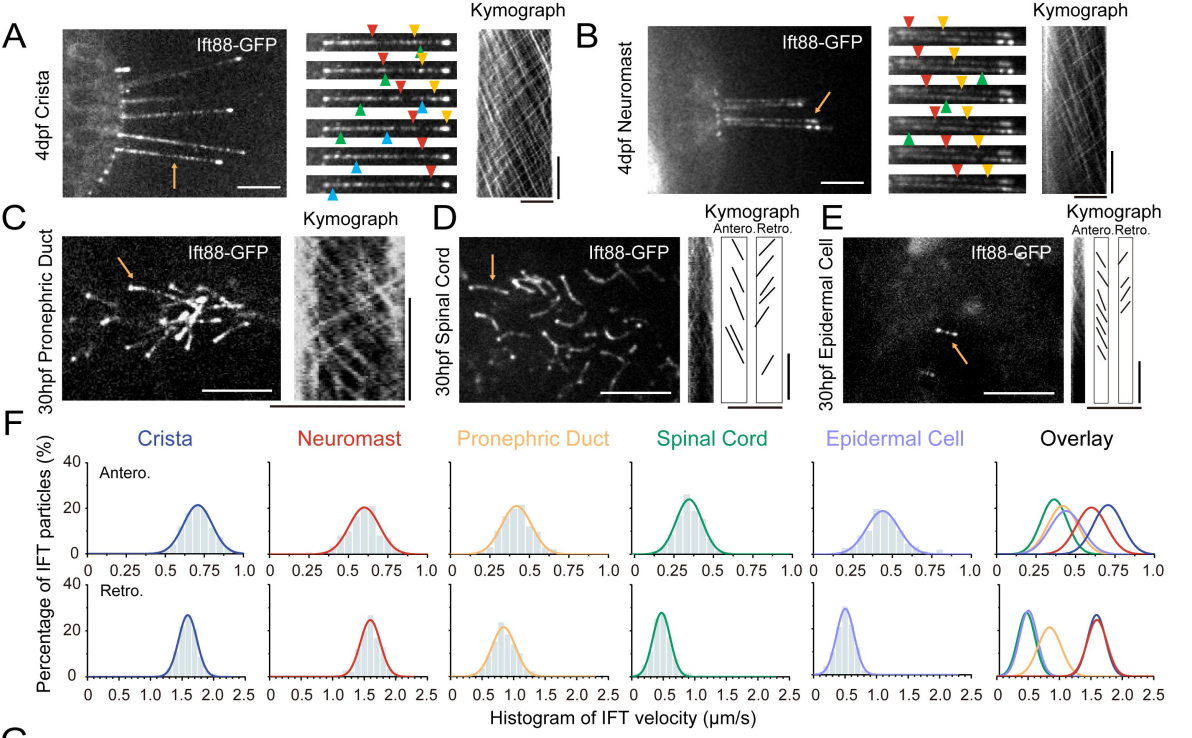

G

IFT average velocities in different tissues (mean ± s.d.,μm/s)

Stages & Tissues	Anterograde	Retrograde	n	N
4dpf Crista	0.68±0.09 (455)	1.55±0.18 (524)	49	17
4dpf Neuromast	0.54±0.10 (194)	1.47±0.19 (300)	27	15
30hpf Pronephric Duct	0.46±0.10 (167)	0.95±0.24 (194)	36	8
30hpf Epidermal Cell	0.42±0.12 (87)	0.56±0.19 (75)	24	9
30hpf Spinal Cord	0.33±0.08 (89)	0.35±0.08 (70)	12	5

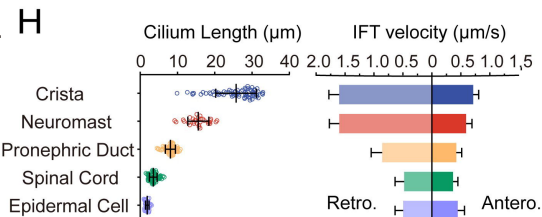

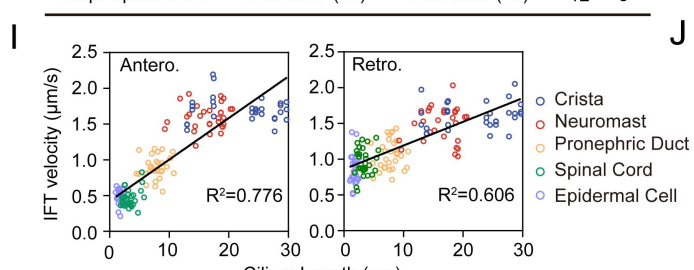

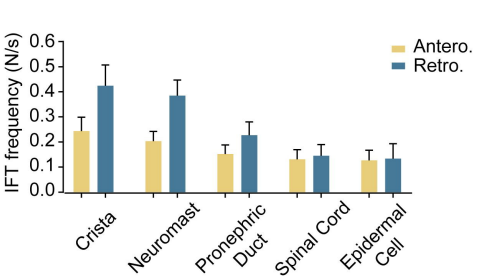

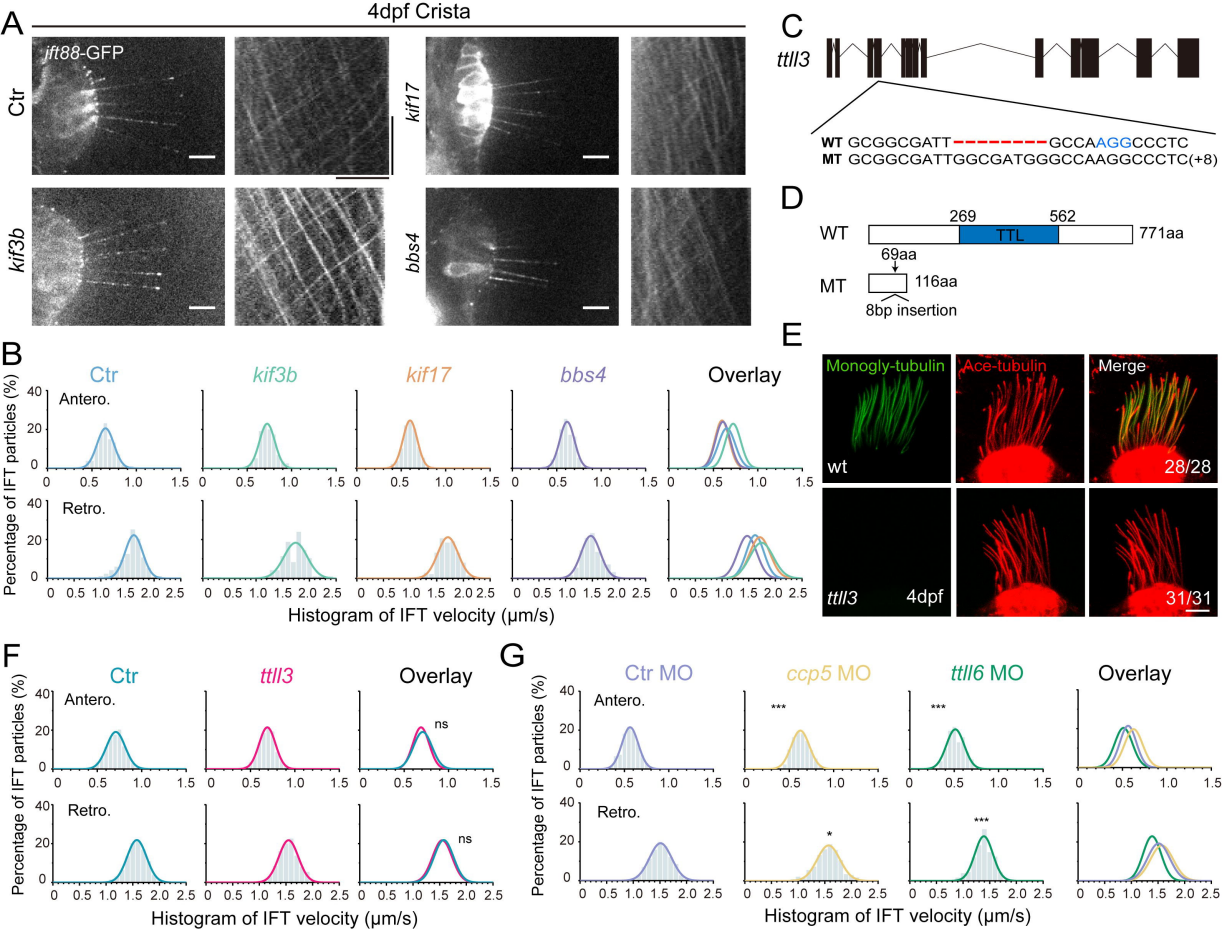
A
4dpf Crista
ift88-GFP
Ctr
kif17
kif3b
bbs4
C
ttll3
WT GCGGCGATT--------GCCAAGGCCCTC
MT GCGGCGATTGGCGATGGGCCAAGGCCCTC(+8)
D
WT
269
562
TTL
771aa
69aa
MT
116aa
8bp insertion
E
Monogly-tubulin
Ace-tubulin
Merge
wt
28/28
ttll3
4dpf
31/31
B
Ctr
kif3b
kif17
bbs4
Overlay
Antero.
Retro.
Percentage of IFT particles (%)
Histogram of IFT velocity (μm/s)
F
Ctr
ttll3
Overlay
ns
G
Ctr MO
ccp5 MO
ttll6 MO
Overlay
***
*

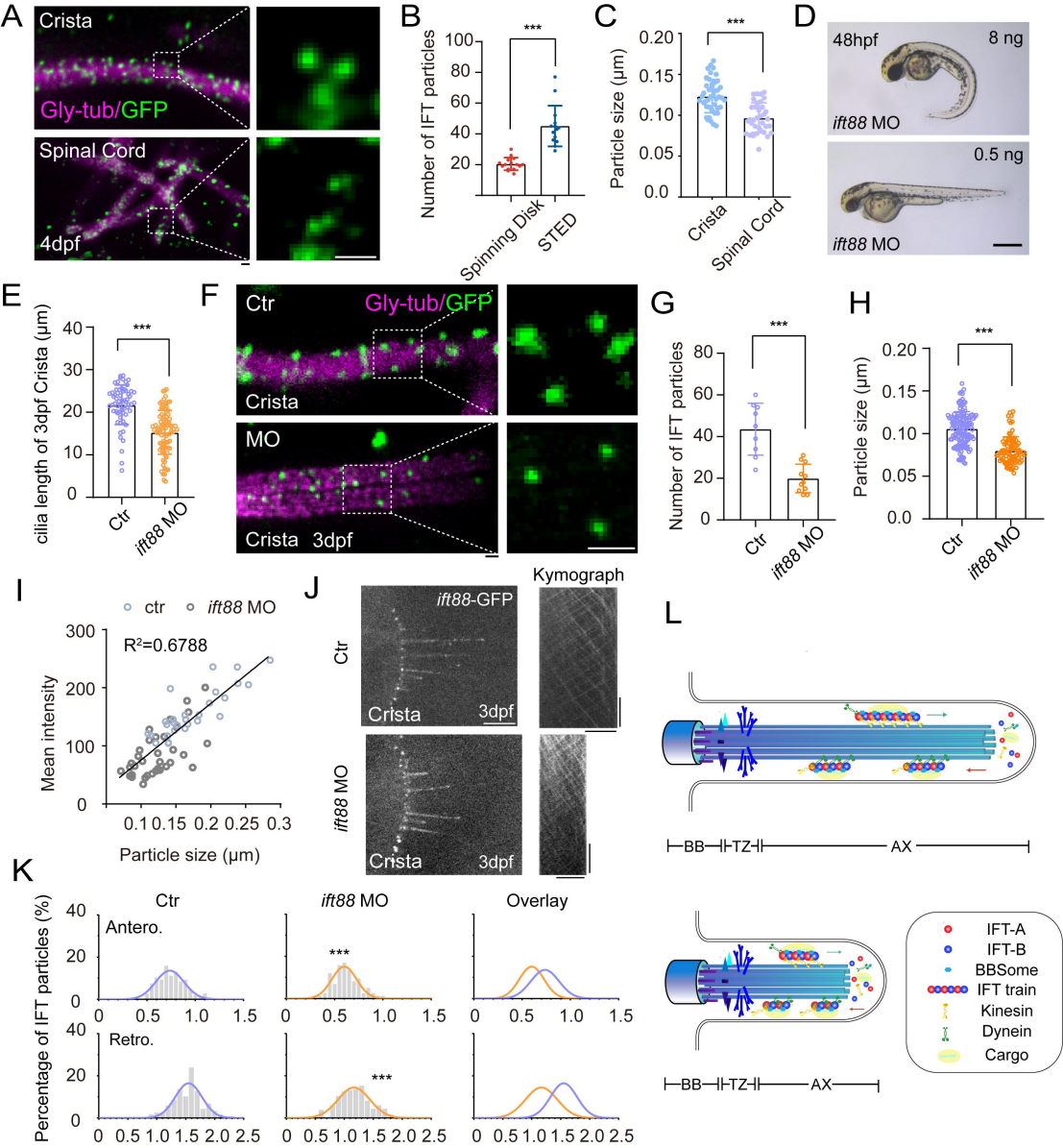
A
Crista
Gly-tub/GFP
Spinal Cord
4dpf
B
Number of IFT particles
***
Spinning Disk
STED
C
Particle size (μm)
***
Crista
Spinal Cord
D
48hpf
8 ng
ift88 MO
0.5 ng
ift88 MO
E
cilia length of 3dpf Crista (μm)
***
Ctr
ift88 MO
F
Ctr
Gly-tub/GFP
Crista
MO
Crista 3dpf
G
Number of IFT particles
***
Ctr
ift88 MO
H
Particle size (μm)
***
Ctr
ift88 MO
I
ctr
ift88 MO
R²=0.6788
Mean intensity
Particle size (μm)
J
Kymograph
ift88-GFP
Ctr
Crista
3dpf
ift88 MO
Crista
3dpf
L
BB
TZ
AX
IFT-A
IFT-B
BBSome
IFT train
Kinesin
Dynein
Cargo
K
Ctr
ift88 MO
Overlay
Antero.
Retro.
Percentage of IFT particles (%)
***
***

A

WT | *ovl*$^{-/-}$ | *ovl*$^{-/-}$; *Tg(hsp70l: ift88-GFP)*

Macula

Ace-tubulin 9/9

Ace-tubulin 5/5

Ace-tubulin/Ift88-GFP 7/7

Olfactory Pit

10/10

6/6

7/7

Pronephric Duct

8/8

10/10

11/11

B

ovl$^{-/-}$; *Tg(hsp70l: ift88-GFP)* | *ovl*$^{+/-}$; *Tg(hsp70l: ift88-GFP)*

♀

♀

♂

♂

A

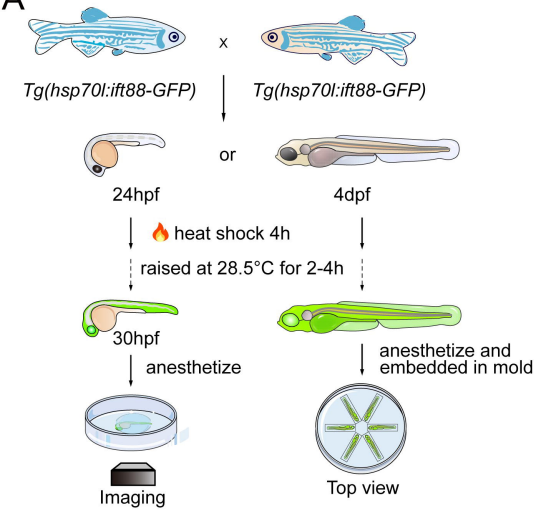

B

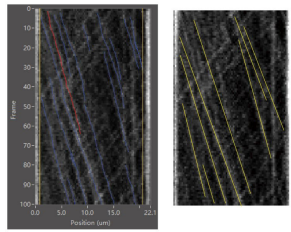

C

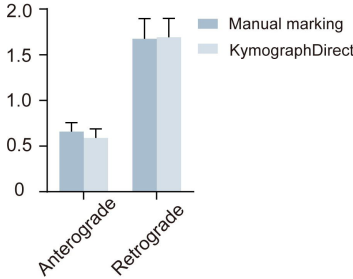

D

IFT Velocities (mean ± s.d.,µm/s)

Method of measurement	Anterograde	Retrograde	n	N
Manual marking	0.66±0.10 (87)	1.67±0.22 (97)	13	3
KymographDirect	0.59±0.10 (84)	1.69±0.20 (59)		

E

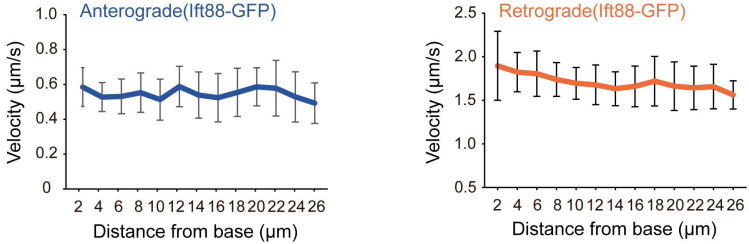

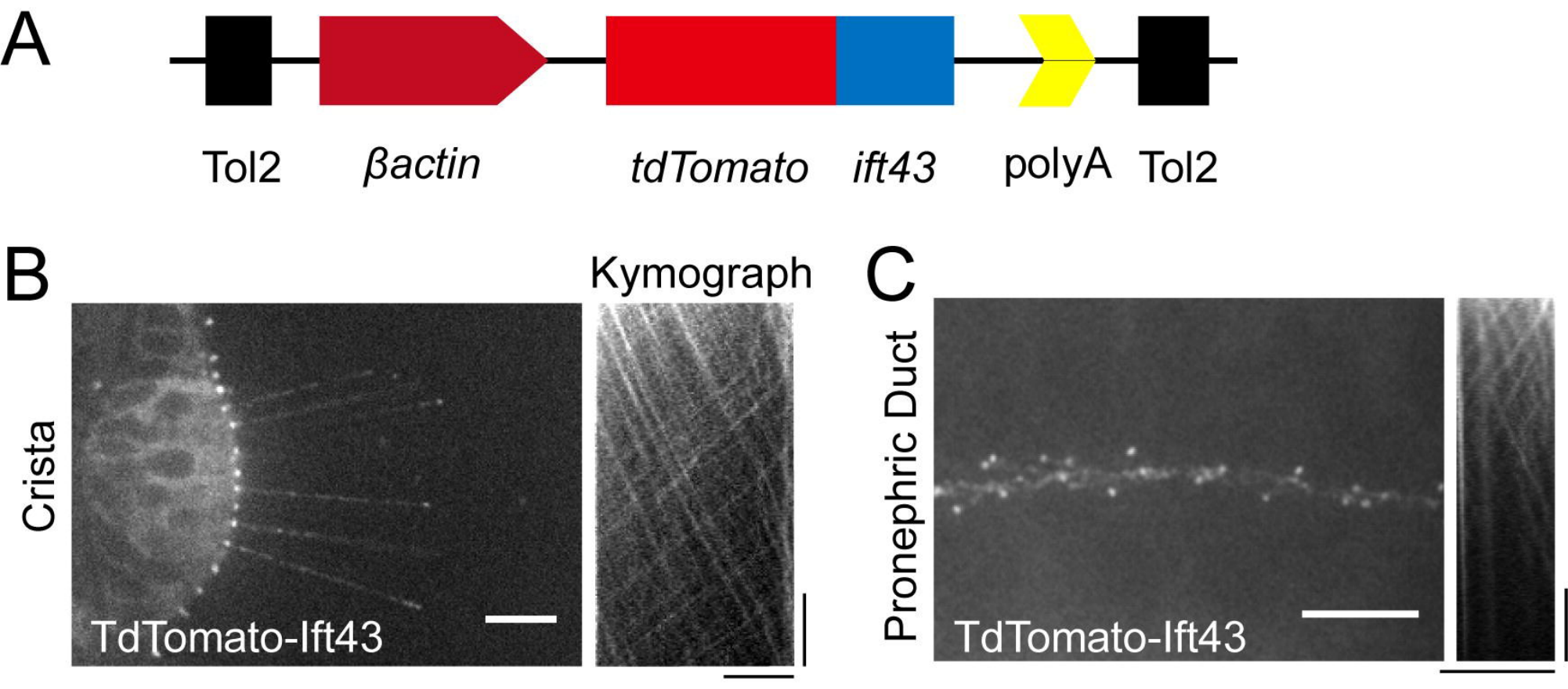

D

IFT Velocities (mean ± s.d.,μm/s)

Stages & Tissues	Anterograde	Retrograde	n	N
4dpf Crista	0.69±0.08 (160)	1.64±0.16 (180)	29	12
30hpf Pronephric Duct	0.39±0.09 (170)	0.78±0.16 (140)	54	8

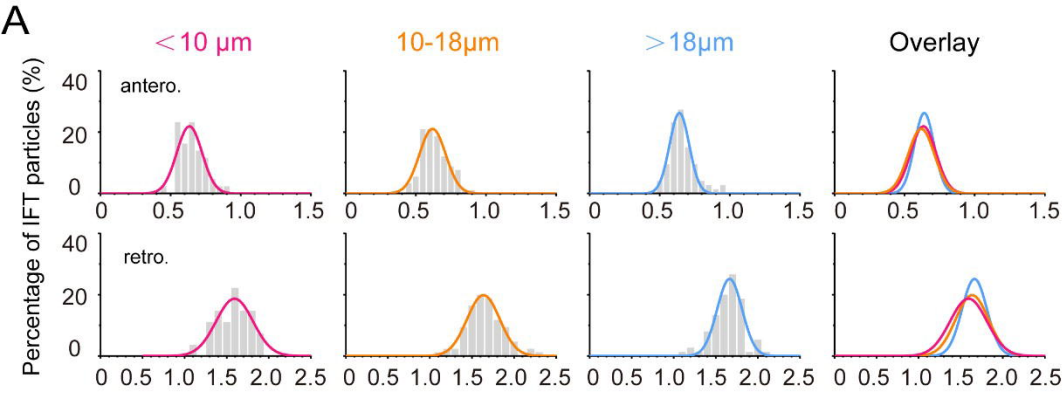

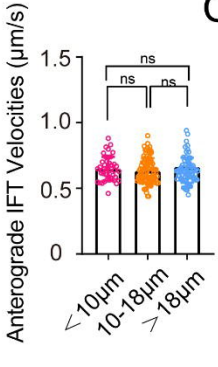

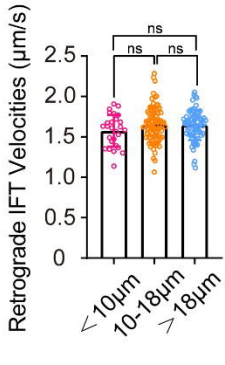

D

IFT Velocities (mean ± s.d.,μm/s)

cilia length	Anterograde	Retrograde
＜10 μm	0.65±0.10 (43)	1.58±0.20 (27)
10-18 μm	0.63±0.10 (91)	1.65±0.22 (85)
＞18 μm	0.66±0.10 (73)	1.65±0.18 (75)

A

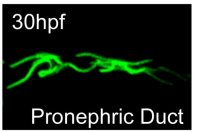

B

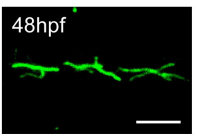

C

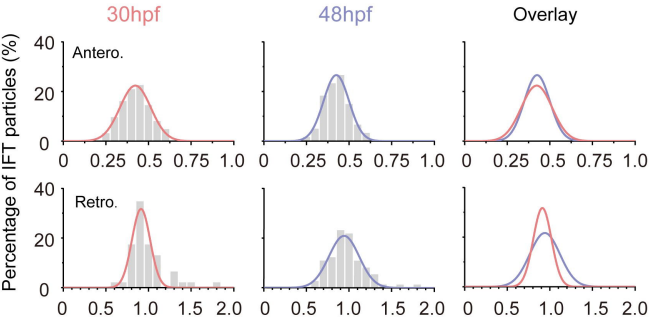

D

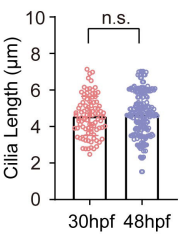

E

IFT Velocities (mean ± s.d.,μm/s)

Developmental stage	Anterograde	Retrograde	n	N
30hpf	0.42±0.08 (62)	0.98±0.21 (46)	14	6
48hpf	0.44±0.09 (61)	0.97±0.21 (73)	18	10

F

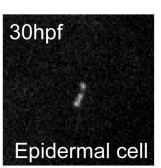

G

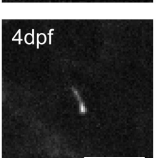

H

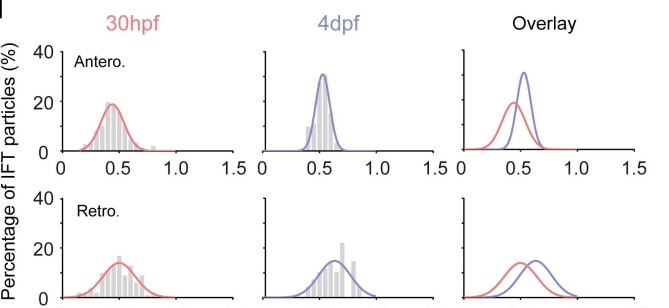

I

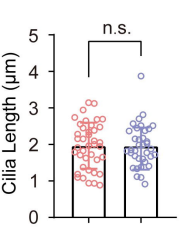

J

IFT Velocities (mean ± s.d.,μm/s)

Developmental stage	Anterograde	Retrograde	n	N
30hpf	0.45±0.12 (148)	0.50±0.14 (101)	42	19
4dpf	0.52±0.07 (91)	0.63±0.12 (68)	35	16

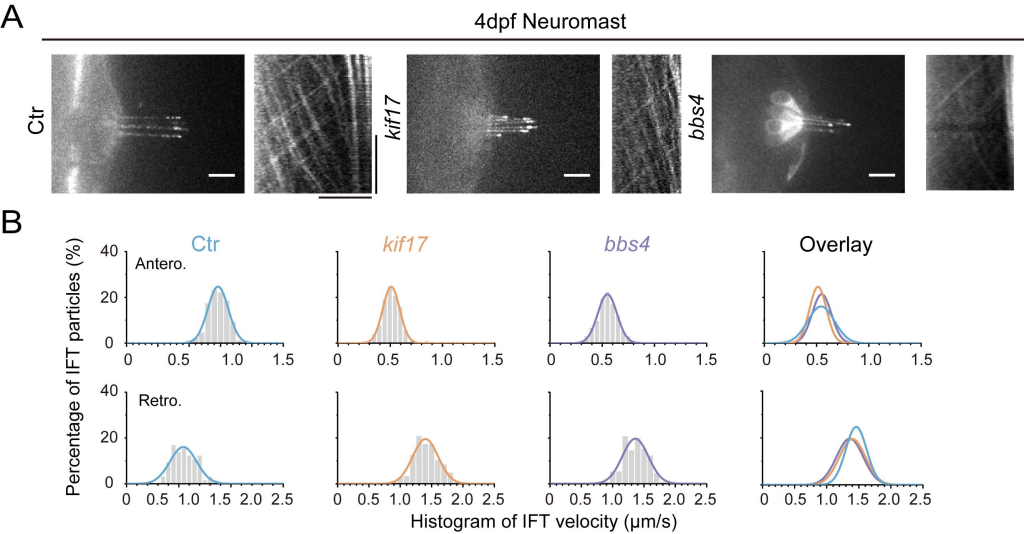
A
4dpf Neuromast
Ctr
kif17
bbs4
B
Ctr
kif17
bbs4
Overlay
Antero.
Retro.
Percentage of IFT particles (%)
Histogram of IFT velocity (μm/s)

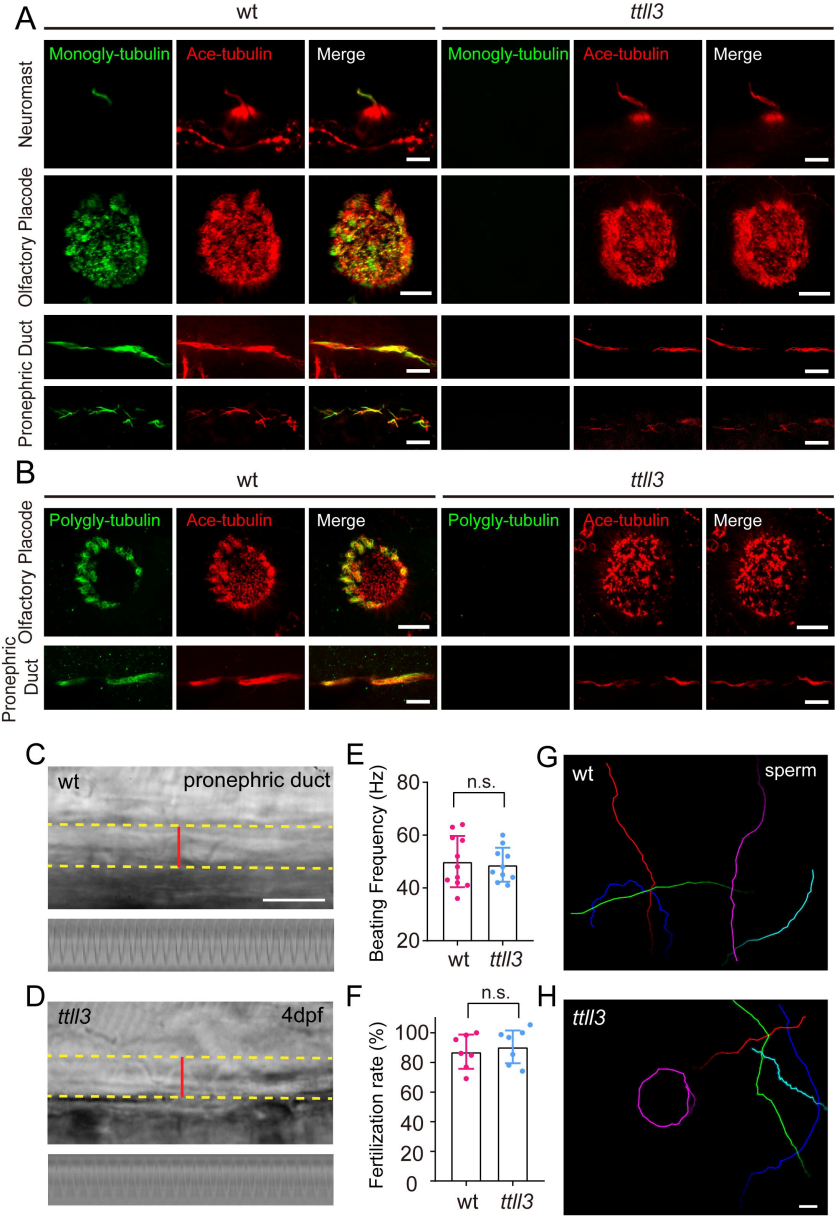
A
wt
ttll3
Monogly-tubulin
Ace-tubulin
Merge
Neuromast
Olfactory Placode
Pronephric Duct
B
Polygly-tubulin
C
pronephric duct
D
4dpf
E
Beating Frequency (Hz)
n.s.
wt
ttll3
F
Fertilization rate (%)
G
sperm
H

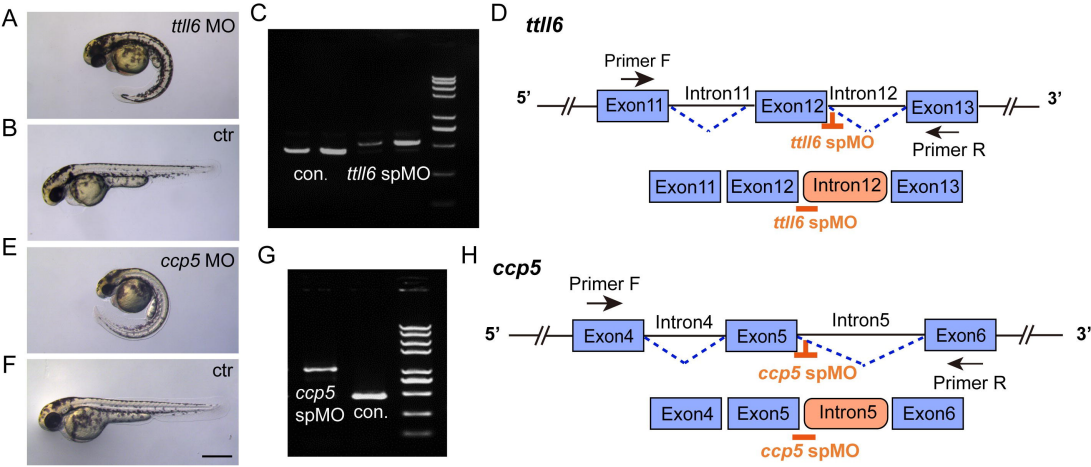
A
ttll6 MO
B
ctr
C
con.
ttll6 spMO
D
ttll6
Primer F
5'
Exon11
Intron11
Exon12
Intron12
Exon13
3'
ttll6 spMO
Primer R
Exon11
Exon12
Intron12
Exon13
ttll6 spMO
E
ccp5 MO
F
ctr
G
ccp5
spMO
con.
H
ccp5
Primer F
5'
Exon4
Intron4
Exon5
Intron5
Exon6
3'
ccp5 spMO
Primer R
Exon4
Exon5
Intron5
Exon6
ccp5 spMO

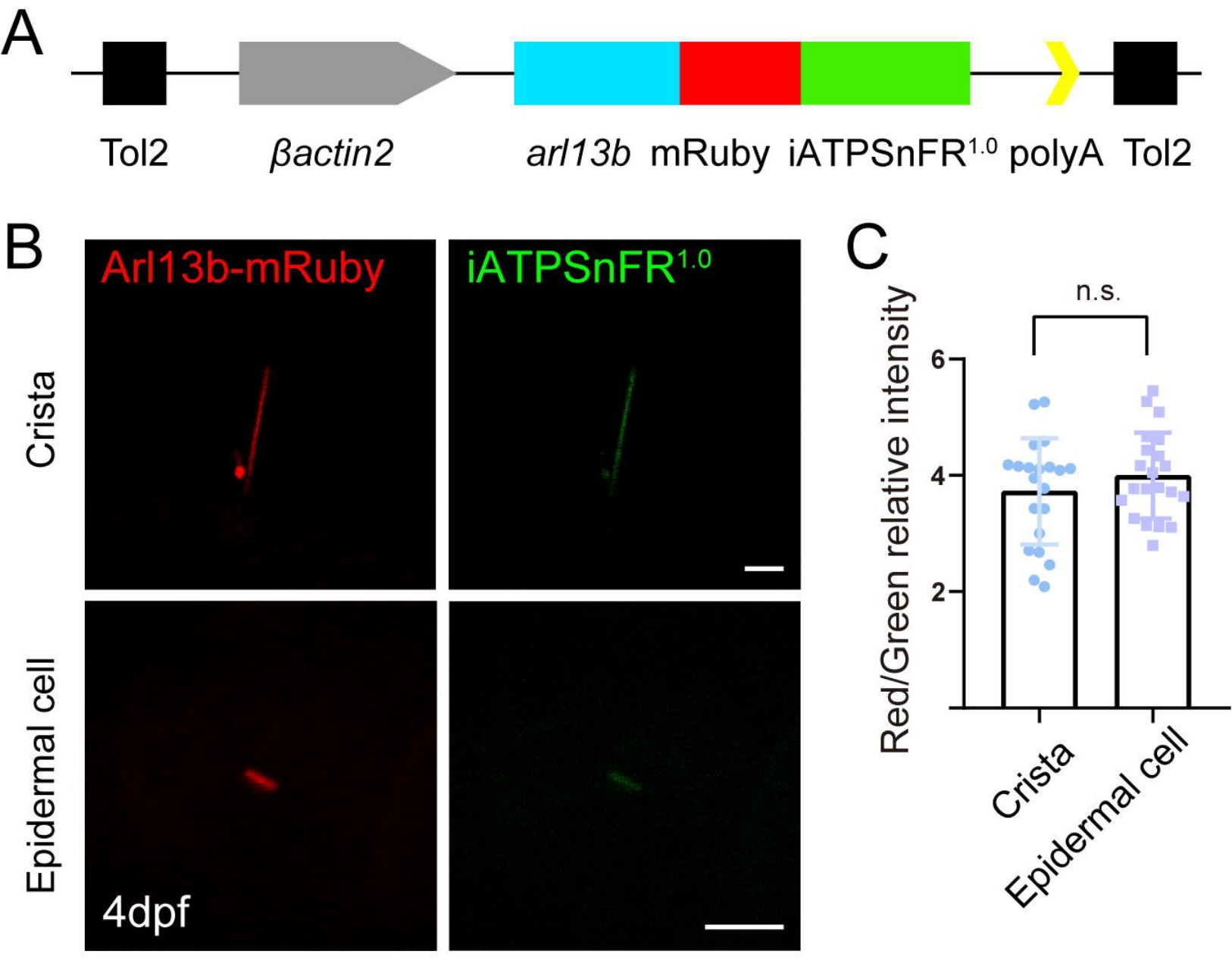
A
Tol2
βactin2
arl13b
mRuby
iATPSnFR1.0
polyA
Tol2
B
Arl13b-mRuby
iATPSnFR1.0
Crista
Epidermal cell
4dpf
C
n.s.
Red/Green relative intensity
6
4
2
Crista
Epidermal cell